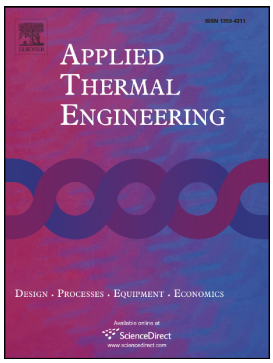

Strategic integration of a biogas-based energy system: Enhancing efficiency and sustainability through demand-side management and battery

Maryam Hasanzadeh, Asgar Minaei, Hadi Ghaebi, Mohammad Ebadollahi, Farkhondeh Jabbari

PII: S1359-4311(25)04116-X

DOI: https://doi.org/10.1016/j.applthermaleng.2025.129524

Reference: ATE 129524

To appear in:

Received date: 16 September 2025

Revised date: 26 November 2025

Accepted date: 16 December 2025

Please cite this article as: M. Hasanzadeh, A. Minaei, H. Ghaebi, et al., Strategic integration of a biogas-based energy system: Enhancing efficiency and sustainability through demand-side management and battery, (2024), https://doi.org/10.1016/j.applthermaleng.2025.129524

Strategic Integration of a Biogas-based Energy System: Enhancing Efficiency and Sustainability through Demand-Side Management and Battery

Maryam Hasanzadeh[a], Asgar Minaei[a*], Hadi Ghaebi[a*], Mohammad Ebadollahi[b*], Farkhondeh Jabbari[c]

[a]Department of Mechanical Engineering, Faculty of Engineering, University of Mohaghegh Ardabili, P.O. Box 179, Ardabil, Iran

[b]Department of Engineering Sciences, Faculty of Advanced Technologies, University of Mohaghegh Ardabili, Ardabil, Iran

[c]Power Systems Operation and Planning Research Department, Niroo Research Institute (NRI), Shahrak Ghods, Tehran, Iran

Corresponding authors: aminaei@uma.ac.ir, hghaebi@uma.ac.ir, m.ebadollahi@uma.ac.ir

Abstract

Due to rapid population growth, increasing fuel costs, and the shift towards renewables, multi-generation systems have emerged as a viable option for producing multiple outputs simultaneously. In this study, the Brayton and inverse Brayton units are utilized as the driving components in the multi-generation structure. The importance of the designed plant lies in the use of renewable biogas fuel and the integration of a Stirling engine (SE) with Brayton and inverse Brayton cycles for waste heat recovery. To recover additional waste heat and produce freshwater, the Multi-Effect Distillation (MED) plant is utilized, while a reverse osmosis (RO) plant produces more freshwater. A cascade absorption–condensation refrigeration cycle is also incorporated to meet the cooling demand. Using EES software, energy, exergy, economic, and environmental analyses are performed on the plant. Additionally, the power generation components are optimized for demand-side management (DSM) and battery energy procurement using GAMS software. According to the results, the proposed system can produce 1684 kW of power, 123.56 kW of cooling, and 10.404 m^3/h of freshwater. The energy efficiency, exergy efficiency, and overall product cost rate are calculated as 51.57%, 50.84%, and 24.93 $/GJ, respectively. The exergy destruction rate is calculated to be 1997.78 kW, and the highest exergy destruction occurs in the combustion chamber. Moreover, the CO_2 emission rate is found to be 299.4 kg/MWh. During peak summer conditions, the electricity generation cost is 65.80 $, but it decreases to 42.00 $ with the integration of a battery system and the implementation of a DSM strategy.

Keywords

Multi-generation system, Energy management, 4E analysis, Demand Side Management, Sustainability.

Nomenclature

A	area (m^2)	HX	Heat exchanger
CDER	CO_2 emission rate, kg/MWh	HPP	High pressure pump
CRF	Capital recovery factor	LHV	Low heat value
D	Demand, (kW)	LNG	liquid natural gas
D_t^{DRP}	Load value after implementation of DRPS, (MW)	Subscripts	
$\dot{E}$	Exergy rate of streams, kW	abs	absorber
FF	Fouling factor	b	brine
h	enthalpy , kJ/kg	com	compressor
MAPE	Mean of Absolute Percent Error	cond	Condenser
MPD	Mean Percent Deviation	ch	Battery charging mode
$\dot{m}$	Mass flow rate, kg/s	che	Chemical
$\dot{n}$	Molar flow rate, mol/s	c. v	Control Volume
P	Pressure , kPa	d	Distilled water
RMSE	Root Mean Square Error	De	Destruction
s	entropy , kJ/kg. K	dis	Battery Discharging mode
SOC	State of charge of battery, (kW)	E. V	Expansion valve
SR	Salt rejection percentage, (%)	Eva	Evaporator
T	Temperature , K	f	Feed water
$\dot{W}$	Electricity , kW	fu	Fuel
$\dot{Z}$	Investment cost rate of components, ($/h)	Gen	Generator
Greek symbols		in	Inlet
η	Efficiency	is	Isentropic
η_{ch}, η_{dis}	Charge and discharge efficiencies	P	Product
ρ	Density of fluid (kg/m^2)	Phy	Physical
Acronyms		RG	Regenerator
CC	combustion chamber	t	time
EES	Engineering Equation Solver		

1-Introduction

1-1- Background and literature review

The worldwide spread of environmental contamination from combined-cycle power plants demonstrates an immediate requirement for renewable fuel adoption, which will decrease our dependence on fossil fuels [1]. The gas turbine (GT) cycle operates as a standard power generation system but it produces substantial amounts of unused thermal energy. Extensive research has focused on methods to recover the waste heat efficiently. The development of biogas-fueled gas turbines has become a major focus because these systems generate cleaner power, while reducing carbon emissions [2]. The following studies highlight recent advances and findings in the application of biogas in GT cycles, illustrating both the technical feasibility and environmental benefits of integrating renewable fuels into conventional power systems.

The biogas-fueled multi-generation system based on a GT was presented by Abdolalipouradl et al. [3]. In this system, the GT, a domestic water heater, a RO system, and a proton exchange membrane (PEM) are integrated to produce power, heating, fresh water, and hydrogen. The study reported thermal and exergy efficiencies of 62.45% and 32.52%, respectively, for the power plant. The

specific cost of electricity was also cited as 28.98 $/GJ. Ersain and Ozgener [4] conducted a thermodynamic study of the ATAER power plant in Turkey. They reported exergy and energy efficiencies of 50.04% and 56%, respectively. The highest exergy destruction was observed in the combustion chamber. Köse et al. [5] investigated waste heat recovery from the GT using both the organic Rankine cycle (ORC) and the steam Rankine cycle. The performance of five working fluids was calculated, and R141b achieved the highest exergy efficiency (67.35%) and thermal efficiency (47.65%). Xie et al. [6] combined an inverse Brayton cycle with a GT cycle and a solid oxide fuel cell (SOFC) to improve energy efficiency. In their configuration, the GT operates under atmospheric pressure, while the SOFC functions near atmospheric pressure. The results showed that when GT compression ratios are 6 and 3, cycle efficiency and power output are improved. This study reported an exergy efficiency of 58.57% for the simulated power. Zoghi et al. [7] compared a combined cycle of a thermoelectric generator, a hot water unit, an absorption chiller, and an inverse Brayton cycle with a simple Brayton combined cycle. In this comparison, the exergy destruction and initial fuel cost were reported to be lower in the first combined-cycle power plant. Furthermore, the plant has an exergy efficiency of 40.77% and an optimal product cost rate of 63.19 $/GJ. Alabdoadaim et al. [8] presented a proposed system including the developed Brayton and inverse Brayton cycles. This study aimed to vary the pressure in the Brayton cycle to find different values of the inverse Brayton cycle pressure. The results showed that the performance is better at high-pressure ratios. This study demonstrates that the proposed cycle with a regenerator achieves the highest efficiency of 49.36%. Chen et al. [9] presented a system consisting of an inverse Brayton with a regenerator and a Brayton cycle with a cooler. In this study, it was found that the regenerator and cooler increase the exergy efficiency within a specific range of pressure ratios. Additionally, increasing the pressure ratio due to the cooler reduces the compressor work. Conversely, decreasing the pressure ratio results in the regenerator saving more fuel. A mathematical model combining the inverse Brayton cycle with a turbocharged diesel engine operating on a dynamic bed was presented by Battista et al. [10]. In this case, the engine efficiency increased by 3.4% at maximum power. Kennedy et al. [11] presented a turbocharged engine that recovered exhaust gas waste heat via an inverse Brayton cycle. Their study showed that GT inlet temperature and system pressure drop significantly affected net power output, with the specific work being approximately 47 kJ/kg. Chen et al. [12] combined the Brayton cycle with a regenerator using finite-time thermodynamics to form an inverse Brayton cycle. They considered system size and flow pressure drop as constraints and optimized the proposed cycle by varying design parameters. These studies indicate that output power is maximized by changing the air flow rate and inlet pressure of the Brayton cycle compressor with a regenerator. Li et al. [13] modeled an inverse Brayton cycle by incorporating a SOFC into their proposed power plant. They considered factors such as steam injection flow rate, compressor pressure ratio, and the lowest plant temperature, resulting in an output power of 39.55 kW and an increase in the SOFC's exergy efficiency to 5.68%. Ebadollahi et al. [14] developed a novel biogas-fueled multi-generation system integrating Brayton/closed Brayton cycles, among others. The system undergoes a holistic 4E and safety analysis. It was also optimized for flexibility in these indicators to serve large industrial facilities. Key results include: 1,864 kW net power; 286.6 kW air conditioning; 75.89 kW cooling; 398.9 kW heating; Freshwater (2.111 kg/s), hydrogen (0.00038 kg/s), biodiesel (0.0088 kg/s), glycerol (0.00091 kg/s).

A Stirling Engine (SE) is employed to generate electrical power while utilizing waste heat from the inverse Brayton cycle. Its suitability stems from several factors: easy start-up, a single-phase working fluid, low noise generation, and the location of its seals and bearings exclusively within the cold region. This makes SE applicable for generating electricity in submarines, ships, and other settings by recovering waste heat from internal combustion engines [15].

Entezari et al. [16] conducted a comparison between a stand-alone GT cycle and a GT cycle with a SE. The results of this study showed that in the combined cycle, output power increases and electricity costs decrease. Compared to the stand-alone GT cycle, the suggested setup improved the exergy efficiency by 16.1%. Alali et al. [17] combined a modular helium reactor cycle with a double-effect absorption chiller and a SE. The waste heat of the modular helium-Bryton cycle powered the refrigeration cycle and the SE. Based on the results, the energy efficiency was increased by about 5.46% at a turbine inlet temperature of 900 °C. Ipci et al. [18] studied an alpha-type SE from the perspective of nodal dynamics and thermodynamics. The engine they considered has a heat transfer area of 3000 cm^2, a swept volume of 1.8 L, and a heat transfer coefficient of 2000 W/m^2K. The hot and cold end temperatures are 1000 K and 400 K, respectively. This type of SE can produce 2 kW at optimal speed, with minimal speed fluctuations and torque.

The imbalance between freshwater demand and supply, industrial expansion, and population growth has led to water scarcity affecting one-quarter of the world's population [19]. The world's available freshwater resources are primarily groundwater and glaciers, which are difficult to access. Additionally, the highest water consumption is in the agricultural sector, which accounts for 70% [20]. Water scarcity is therefore one of the world's most pressing fundamental challenges, necessitating significant technological advancement to produce freshwater. Desalination, particularly efficient methods like RO, offers a viable solution to compensate for freshwater shortages by utilizing alternative water sources. The following studies investigate RO desalination [21]. Chandio et al. [22] proposed a cycle that combined an ORC cycle with RO desalination. This study was conducted to recover excess heat and waste gases from the exhaust of an internal combustion engine. The simulated plant was examined in terms of thermodynamic studies, including exergy, economics, and energy. The proposed plant was capable of producing 195.9 kW of net power and 19.74 m^3/h of fresh water. Also, the exergy efficiency of this plant was reported to be 65.19%, and its energy efficiency is 68.14%. Li et al. [23] simulated a combined cycle power plant that produced hydrogen, electricity, and fresh water. In their design, an ORC cycle generated electricity, a PEM cell produced hydrogen, and an RO cycle handled desalination. In the optimal case, the cycle produced 5092 kW of power, achieved an exergy efficiency of 43.55%, and produced 41.75 kg/s of fresh water. El-Ashmawy et al. [24] designed three nuclear power plant-desalination plant configurations and investigated them from a thermo-economic perspective. According to the results, the RO unit was found to be more cost-effective than thermal desalination. The MED-RO plant is 0.36 $/m³ less cost-effective than the Multi-Stage Flash Distillation (MSF)-based plant.

Thermal desalination plants account for about 27% of the world's freshwater plants [25]. One type of thermal desalination plant is the MED plant, which requires less energy than other methods and has lower capital costs. To protect the environment, renewable energy can be utilized to produce

freshwater in such plants. Today, due to the growing global demand for freshwater, studies on desalination plants are increasing.

Chitgar et al. [26] integrated a hydrogen production cycle with geothermal and desalination systems. They considered two scenarios, one with a MED plant and the other with a RO plant. The results showed that the configuration with a RO had a higher water production efficiency. In contrast, the configuration designed with a MED plant had better economic benefits. Musharavati et al. [27] described a gasifier-based power plant as a MED unit with thermal vapor compression, a combustor, and a GT compressor. In this study, 38.6 kg/s of fresh water and 5127 kW of net power were produced at the optimum points. Additionally, the optimum exergy efficiency was 15.61%, and the total cycle cost rate was 206.78 $/h. Another result showed that the number of MED plant effects does not affect the carbon dioxide emission rate. Xu et al. [28] proposed a new multi-generation power plant to produce heat, cooling, freshwater, and electricity. The cycle includes a MED plant, an absorption chiller, an LNG cycle, an ORC, and a biomass-fueled combustor. The cycle could produce 1743 kW of heating, 4927.4 kW of cooling, 19.83 kg/s of drinking water, and 10403 kW of net electricity. The exergy efficiency was also calculated to be 37.15%, and the energy efficiency was 67.1%. In addition, the product cost rate was 14.89 $/GJ, and the total cost rate was 568 $/h. Liu et al. [29] presented a mathematical model, the state-space superstructure, to design an optimal MED system that improves the plant's thermal performance. Their model increased the output efficiency ratio by 16% compared to feed-forward arrangements and enhanced freshwater production capacity. Separately, Shahzad et al. [25] developed a MED plant model incorporating an adsorption cycle. Their study compared the water production rate of this hybrid MED unit with that of a conventional system, noting that the improved design extracts heat from ambient air and operates at sub-ambient temperatures. The results indicated that higher brine concentration in subsequent effects stems from increased water recovery, while lower saturation temperatures in these stages reduce sedimentation effects.

To optimize the production capacity of the proposed cycle, GAMS software is used, and two operating scenarios are considered: one without battery storage and DSM, and one with battery storage and DSM. Related studies are summarized below. In this field, Jabbari et al. [30] present a novel trigeneration power plant comprising combined heat and power generators, a RO unit, a dehumidification cycle, and a gravity energy storage system. Four scenarios are considered for energy management, including gravity energy storage, demand-side management, and an economic dispatch strategy. The goal is to minimize the total production cost of the system over a 24-hour study period. To address the challenges of real-time optimization, Zhang et al. [31] proposed an Internet-based distributed energy management strategy. Their strategy was developed for plug-in hybrid electric vehicles and has a two-layer structure. In their study, experiments were conducted under critical conditions, such as grid failures and heavy computational loads. Qi et al. [32] addressed the issues of module overheating and insufficient thermal balance in automotive batteries under high discharge rates by proposing an innovative cooling belt mechanism for cylindrical lithium-ion batteries, based on the temperature distribution characteristics within battery modules. A comparative analysis of the thermal–hydraulic performance of four cooling structures demonstrated that the proposed design provided superior efficiency in battery thermal management applications. To address the problem of reduced vehicle battery life and decreased occupant safety

caused by the large amount of heat generated in high-energy-density vehicle batteries at high discharge rates, Qi et al. [33] proposed a multi-U-style microchannel liquid cooling plate (Multi-U), based on the heat generation and temperature distribution characteristics of vehicle batteries. The results showed that the cooling performance is better with the side-face arrangement. Furthermore, through comparative analysis with a conventional spiral microchannel cold plate and a parallel microchannel cold plate, the Multi-U configuration exhibited better overall performance.

In the existing literature, single-generation, cogeneration, trigeneration, and multi-generation systems have been investigated. Key findings are summarized in Table 1, which also reports the optimization approaches employed in these studies. In particular, Table 1 highlights optimization methods based on demand-side management and battery energy procurement that have recently been applied to multi-generation systems to determine the extent to which the objective function can be achieved under optimal operating conditions.

Table 1: Overview of Optimization and Performance Analyses in Existing Multi-/Tri-/Single-Generation Studies

Authors	Type	Energy	Exergy	Economic	Environmental	Energy management	Optimization	Observation
Goodarzi et al. [34]	Single	+	+	-	-	-	-	The new regenerative Brayton–Inverse Brayton cycle showed higher net power and less sensitivity to compressor pressure ratio.
Li et al. [13]	Single	+	+	-	-	-	-	The addition of inverse Brayton cycle increased net power, fuel consumption, and reduced exergy destruction.
Prajapati et al. [35]	Single	+	-	-	-	-	Multi-objective optimization	HTS optimization achieved a maximum specific work of 497 kJ/kg with an efficiency of 44%.
Abrosimov et al. [36]	Single	+	-	+	-	-	levelized cost of energy optimization	inverse Brayton with ORC achieves 10% higher efficiency; optimized levelized cost of energy 159.5 $/MWh vs 169.8 for regenerative ORC.
Hou et al. [37]	Single	+	+	+	-	-	Multi-objective optimization	The exergy efficiency, heat exchanger area per unit output power, and its levelized energy cost were obtained as 55.68%, 0.115. m^2/kW, and 4.23 cents/(kWh), respectively.
Zhou et al. [38]	Co*	+	+	+	-	-	Multi-objective optimization	Combined system achieves 37.98% exergy efficiency and levelized cost of energy 79.96 $/MWh, improving baseline by 11.9–14.5%.
Li et al. [39]	Co	+	+	-	-	-	Multi-objective optimization	Solid oxide thermal power plants with integrated HX grid achieved electrical efficiencies of over 50% and complete CO_2 capture.
Yang et al. [40]	Tri	+	-	+	-	-	Multi-objective optimization	Heating-mode index up to 31% higher; cooling benefit only in θ=1.37–1.53.
Nondy et al. [41]	Tri	+	+	+	+	--	Multi-objective optimization	The optimization reduced costs by 8 to 9 % and greenhouse gas emissions by 1.5 to 2 %.

Mahdavi et al. [42]	Tri	+	+	+	+	-	Multi-objective optimization	Optimization increases exergy 46.85→53.22% and reduces cost 175→157 $/h; Kalina has highest destruction.
Colakoglu et al. [43]	Multi	+	+	-	+	-	Multi-objective optimization	Energy efficiency was 55.57%, exergy was 39.45%; also 252 kW of electricity, 95.5 kW of heating, 175.8 kW of hot water consumption, 19.5 kW of cooling, and 0.559 kg/h of hydrogen were obtained.
Ebadollahi et al. [14]	Multi	+	+	+	+	-	Multi-objective optimization	The unit cost of the product, exergy efficiency, environmental impact of the product is 1.828, 40.58 $/GJ, 31.11%, 6232 mP/GJ, and 1656 $/year.
Zoghi et al. [7]	Multi*	+	+	+	+	-	-	The multi-generation design recovered more waste heat and simultaneously produced electricity, hydrogen, and fresh water with higher exergy efficiency.
*Co: Cogeneration, Tri: Trigeneration, Multi: Multigeneration								

1-2- Objectives

In this study, considering the green transition, renewable biogas is used as a fuel in the Brayton cycle. One of the key advantages of the system is the use of biogas as a fuel for electricity generation. Biogas also prevents environmental damage, a key design goal of the proposed system. The gas flow velocity through a GT is significantly higher than that of a diesel engine. Furthermore, if the airflow in a conventional device becomes supersonic, a shock wave may be generated, leading to material damage and energy loss. In the new Brayton and inverse Brayton cycles, the extraction of high-energy exhaust air from the combustion chamber is regulated. It is then fed into the downstream inverse Brayton cycle to produce net power output. The main advantage of the Brayton cycle is that some work is produced during expansion, which can be used to drive the cycle compressor. Nevertheless, because the working fluid does not undergo a phase change throughout the cycle, it is necessary to increase the air mass flow rate to achieve the required cooling rate. A SE is used to recover the excess heat from the Brayton and inverse Brayton cycles. The SE is a reliable and easy-to-maintain technology used to power the RO desalination plant. Additionally, the MED plant is utilized to recover the waste heat from the Brayton cycle. Finally, the cascade absorption-condensation refrigeration cycle is used to produce cooling.

1-3-System innovations

- Using renewable biogas fuel in the Brayton and inverse Brayton power generation cycle is designed in a novel multi-generation structure
- Optimizing the power generation of the Brayton and inverse Brayton cycle with GAMS software
- Investigating the carbon dioxide emission rate of the proposed cycle and finding the most influential design parameter on its emission rate

- Optimal use of two desalination models to prevent cycle waste heat
- Using a SE at the output of the inverse Brayton cycle to provide power for the RO desalination plant
- Applying the DSM and battery strategies for the multi-generation system

Figure 1 presents a simplified flow diagram of the proposed multi-generation SYSTEM, which is based on a combination of biogas-fired Brayton and inverse Brayton cycles, a SE, a RO unit, a MED unit, and a cascade absorption–condensation refrigeration cycle.

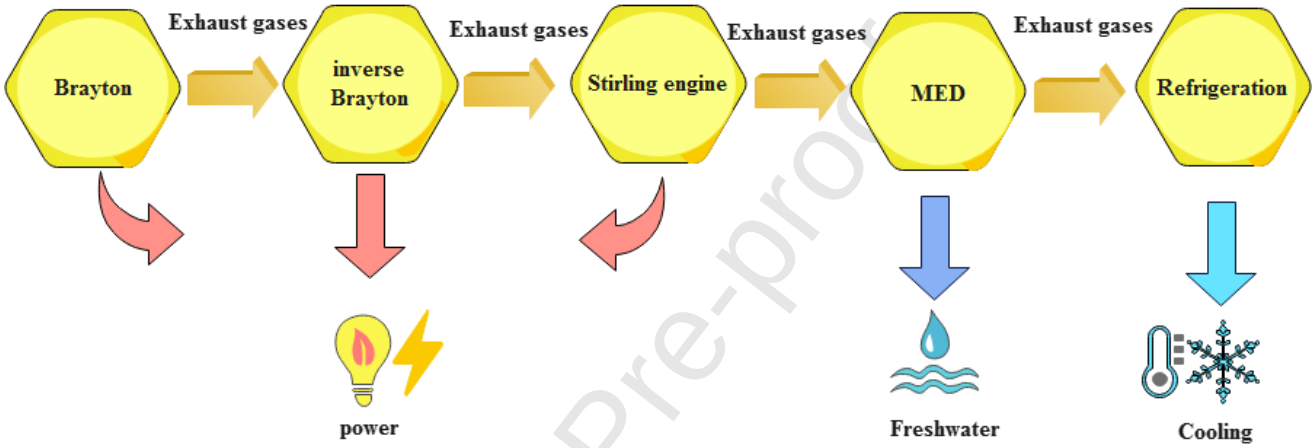

Figure 1: Simple flow chart of the proposed multi-generation cycle

2- **System description**

The simulated system in this study comprises a combined cycle consisting of a Brayton cycle, an inverse Brayton cycle, a SE, a MED plant, a RO plant, and a cascade absorption-condensation refrigeration cycle. The schematic of the proposed system is shown in Figure 2.

2-1- Brayton and inverse Brayton cycles

The Brayton cycle (upper system) supplies energy to the inverse Brayton cycle (lower system). The process begins with air entering the Brayton cycle compressor, where it is compressed to the cycle's maximum pressure. The pressurized air passes through a regenerator to preheat it before entering the combustion chamber. In the Brayton cycle combustor, heat is added to the air until the maximum cycle temperature is reached. High-temperature exhaust gas from the combustor powers the Brayton cycle turbine, which in turn drives the compressor. After expansion in the turbine, the exhaust gas passes through the regenerator to preheat the incoming air. The exhaust gas then enters the inverse Brayton cycle, where it is further expanded at atmospheric conditions to enhance power generation and efficiency. In the inverse Brayton cycle, the expanded gas undergoes constant-pressure cooling, followed by compression driven by the inverse Brayton cycle turbine. The inverse Brayton cycle provides the net power output. A heat exchanger is installed between the Brayton and inverse Brayton power generation cycles to reduce the power consumption of the inverse Brayton cycle

compressor. In addition, following discharge to the atmosphere, the cooled gas stream enters the inverse Brayton cycle compressor.

2-2- SE system

In order to recover the waste heat of the inverse Brayton cycle, the SE is used. The volume, temperature, and pressure of the helium working fluid in the SE change in response to heat transfer. The SE provides the power for the RO desalination cycle by converting the Brayton cycle's waste heat into work. In the Stirling engine, the right piston contains the helium working gas, and the heat source in the first stage is heated and transfers heat to the helium. At this stage, the piston begins to move due to the pressure generated by the heated helium, thereby producing power. In the next stage, the cold piston moves upward while the hot piston moves downward. The motion of the cold piston is driven by heat transfer to the low-temperature section of the heat exchanger and by the flow of the helium working fluid toward this section. The helium working fluid is compressed by a piston located in the cold cylinder section. In the final stage, the hot and cold pistons move downward and upward, respectively, and their motion is simultaneous. The final step is to push the heated helium working fluid into the hot cylinder and repeat the cycle.

2-3- MED cycle

In the present study, a MED plant was used to recover heat from exhaust gases. First, at point 10, the exhaust gas stream leaving compressor 2 enters the MED heater and leaves as a lower-energy stream at point 11. Meanwhile, all seven effects of the MED desalination plant operate under the same operating conditions. Next, at point 12, seawater enters the desalination condenser, where it is heated and then leaves at point 13. Stream 13 then splits into streams 14 and 15. To enhance freshwater production at point 33, additional seawater is supplied to the condenser. After condensation, at point 14, seawater returns to the sea. Outlet stream 15 is divided into streams 16 through 22. In the first stage, stream 22 enters the first-effect hot tubes, causing partial evaporation of the seawater. The resulting steam exits at point 25 and is directed to the second effect, while the brine leaves at point 26. Steam from point 25 continues to the second effect, where it evaporates seawater at point 21 and condenses at point 27, producing freshwater, while the remaining brine exits at point 29. The steam from point 28 then enters the third effect, continuing the desalination process. The produced steam heat is directed into the desalination condenser at point 33. Freshwater is collected at point 46 in the reservoir, while brine is removed at point 44.

In the present study, the last stage of exhaust gas heat recovery utilized cascade absorption-condensation refrigeration to produce cooling.

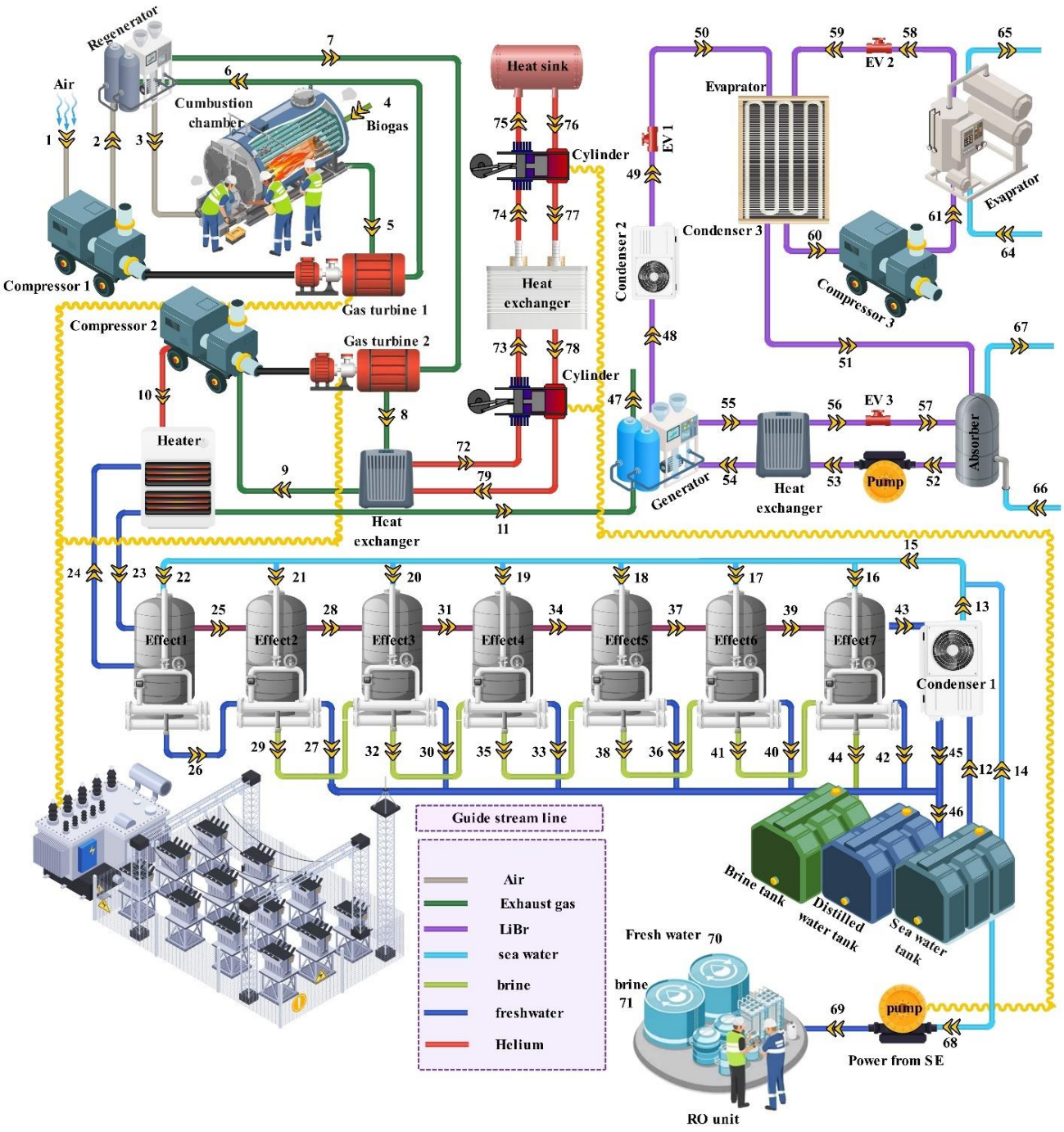

Figure 2: Schematic of the biogas-fired multi-generation system based on Brayton and inverse Brayton cycles, a Stirling engine, a MED unit, a Ro plant, and a cascade absorption–condensation refrigeration cycle

3-Modeling assumptions

This section on modeling assumptions, based on thermodynamic laws, presents the assumptions employed in simulating the proposed cycle. It then proceeds to discuss the mathematical models of the cycle components, including the Brayton and inverse Brayton cycles, the MED plant, and the

RO cycle. The cycle simulation was performed in EES, and energy consumption was analyzed in GAMS. The specific modeling assumptions for the proposed system are as follows:

- The ideal gas laws are used for air and combustion products [44].

- The combustion is considered complete, and the air composition is assumed to be 21% oxygen and 79% nitrogen [45].

- The system is assumed to be in adiabatic condition [46].

- In the MED desalination plant, there are 7 distillation stages, and the brine temperature exiting the first stage is assumed to be 343.75 K [47].

-The flow exiting the evaporators and condensers is assumed to be saturated [48].

-Constant isentropic efficiency is assumed for compressors and turbines [49].

- A steady state is considered for all flows [50].

- The ambient pressure is 101.3 kPa and the ambient temperature is 25°C.

The design parameters used in the proposed multiple production cycle are presented in Table 2.

Table2: Input parameters of multi-generation system

Parameters	Data	Unit
Brayton & inverse Brayton cycle [35]		
Brayton cycle compressor inlet air temperature	293.15	K
Turbine inlet air temperature	1300	K
Compressor Pressure Ratio 1	5	-
Compressor Pressure Ratio 2	1.3	-
Isentropic efficiency of compressors	0.8	-
Isentropic efficiency of gas turbine	0.88	-
Gas turbine inlet temperature 1	650	K
Inverse Brayton cycle turbine outlet pressure	35	kPa
Stirling engine [16]		
Power piston effectiveness	0.91	-
Heat sink temperature	303.15	K
The working fluid's mole	1	kmol
RO unit [23]		
Recovery ratio	28	%
Number of pressure vessels	40	-
Salt rejection content	0.99	-
Element area	33.5	m^2
MED cycle [51]		
Inlet seawater temperature	303.15	K
Content of salt in seawater	0.038	-
Number of effects	7	-
Steam inlet temperature to the first effect	344.5	K
Condenser temperature difference	276.25	K
Temperature difference between effects	276.43	K
Refrigeration cycle [52]		

Temperature of Evaporator	278.65	K
Efficiency of Pump	0.8	-
The temperature of the dilute solution exiting the adsorption	309.15	K
Efficiency of Compressor	0.8	-

3-1-Mathematical model of the Brayton and inverse Brayton cycles

The temperature rise of air entering compressor 1, accounting for its isentropic efficiency in the Brayton cycle, is calculated as follows [34]:

$$T_2 = T_1\left(\frac{P_2}{P_1}\right)^{\frac{k-1}{k\eta_{com1}}} \quad (1)$$

In the above relationship, "k" represents the specific heat ratio. Isentropic efficiency, defined for compressors, is calculated as below [34]:

$$\eta_{com1} = 1 - \left(0.04 + \frac{R_{com1} - 1}{150}\right) \quad (2)$$

R_{com1} in the above equation represents the compression ratio of the compressor1, which is calculated according to the following equation [53]:

$$R_{com1} = \frac{P_2}{P_1} \quad (3)$$

The work consumed by the compressor 1 is defined as follows [53]:

$$\dot{W}_{com1} = \dot{m}_{air}(h_2 - h_1) \quad (4)$$

The combustion products exiting the combustion chamber are defined by the molar flow rate of air and the molar flow rate of fuel as follows [54]:

$$\bar{\lambda} = \frac{\dot{n}_{fu}}{\dot{n}_{air}} \quad (5)$$

$\bar{\lambda}$ in the above equation, represents the molar ratio of fuel to air moles, which is expressed as follows [54]:

$$\frac{\dot{n}_p}{\dot{n}_{air}} = 1 + \bar{\lambda} \quad (6)$$

Biogas combustion, which contains 60% methane and 40% carbon dioxide, is expressed by the following chemical reaction [54]:

$$\bar{\lambda}[0.6CH_4 + 0.4CO_2] + [0.7748N_2 + 0.2059O_2 + 0.0003CO_2 + 0.019H_2O] \rightarrow [1 + \bar{\lambda}][Y_{N_2}N_2 + Y_{O_2}O_2 + Y_{CO_2}CO_2 + Y_{H_2O}H_2O] \quad (7)$$

The mole fraction of carbon, hydrogen, nitrogen, and oxygen is defined through the gas balance as follows [54]:

$$Y_{CO_2} = \frac{\bar{\lambda} + 0.0003}{1 + \bar{\lambda}} \quad (8)$$

$$Y_{H_2O} = \frac{1.2\bar{\lambda} + 0.019}{1 + \bar{\lambda}} \quad (9)$$

$$Y_{N_2} = \frac{0.7748}{1 + \bar{\lambda}} \quad (10)$$

$$Y_{O_2} = \frac{0.2059 - 1.2\bar{\lambda}}{1 + \bar{\lambda}} \quad (11)$$

By applying the energy balance to the combustion chamber, the following equation is obtained as [54]:

$$\dot{Q}_{c.v} + \dot{n}_{fu}\bar{h}_{fu} - \dot{n}_p\bar{h}_p + \dot{n}_{air}\bar{h}_{air} = 0 \quad (12)$$

The rate of heat transfer in the combustion chamber is defined according to the following equation [54]:

$$\dot{Q}_{c.v} = -0.02\dot{n}_{fu}\overline{LHV} \quad (13)$$

By integrating the two equations above, the following relationship is obtained [54]:

$$\bar{\lambda}\bar{h}_{fu} - (1 + \bar{\lambda})\bar{h}_p + \bar{h}_{air} = 0.02\bar{\lambda}\overline{LHV} \quad (14)$$

Also, the temperature of the exhaust gases from Gas Turbine 1 is calculated as follows [54]:

$$\frac{T_5}{T_6} = \left(\frac{P_5}{P_6}\right)^{\frac{(k-1)\eta_{GT1}}{k}} \quad (15)$$

The isentropic efficiency of Gas Turbine 1 is expressed by the following equation [54]:

$$\eta_{GT1} = 1 - \left(0.03 + \frac{R_{GT1} - 1}{180}\right) \quad (16)$$

Power generation by Gas Turbine 1 is defined as the following equation [54]:

$$\dot{W}_{GT1} = \dot{m}_p(h_5 - h_6) \quad (17)$$

The exhaust gas temperature of an inverse Brayton cycle gas turbine (Gas Turbine 2) and its output power are defined by the following equation [54]:

$$\frac{T_7}{T_8} = \left(\frac{P_7}{P_8}\right)^{\frac{(k-1)\eta_{GT2}}{k}} \quad (18)$$

$$\dot{W}_{GT2} = \dot{m}_p(h_7 - h_8) \quad (19)$$

The work consumed by the compressor 2 and the temperature of its exhaust gases are reported as [54]:

$$\frac{T_{10}}{T_9} = \left(\frac{P_{10}}{P_9}\right)^{\frac{(k-1)}{k\eta_{com2}}} \quad (20)$$

$$\dot{W}_{com2} = \dot{m}_p(h_{10} - h_9) \quad (21)$$

The net output work of the Brayton and inverse Brayton cycles is defined as follows [54]:

$$\dot{W}_{net} = \dot{W}_{GT1} + \dot{W}_{GT2} - (\dot{W}_{com1} + \dot{W}_{com2}) \quad (22)$$

The efficiency of the Brayton and inverse Brayton cycles is calculated as follows [54]:

$$\eta_{cycle} = \frac{\dot{W}_{net}}{\dot{m}_{fu} \times LHV} \quad (23)$$

3-2-Mathematical model of MED cycle

The heat transfer equation inside the boiler of the MED cycle is calculated as [55]:

$$\dot{Q}_{in,MED} = \dot{m}_{hw}C_{p,hw}(T_{24} - T_{23}) = \dot{m}_{10}(h_{10} - h_{11}) \quad (24)$$

The specific heat capacity of hot water is represented by $C_{p,hw}$. Also, the following equation shows the mass flow rate of feed water (f_i) for stage i [55]:

$$f_i = \frac{F}{N} \quad (25)$$

N is the number of desalination effects. In order to calculate the mass flow rate of the steam formed (D_i), the following equation is presented [55]:

$$\sum_{i=1}^{N} D_i = D_t \quad (26)$$

For stages 1 to N, the energy balance is defined as the following equations [56]:

$$\Delta T = \frac{T_S - T_N}{N} \quad (27)$$

$$T_1 = T_S - \Delta T \quad (28)$$

$$T_{i+1} = T_i - \Delta T \qquad i=1, \ldots, N-1 \quad (29)$$

In order to write the energy and mass balance for the condenser, the following equation is used [56]:

$$T_f = T_N - \Delta T_{cond} \quad (30)$$

3-3-Mathematical model of RO desalination cycle

The reverse osmosis unit is used to desalinate the feed water. The following expression is used to determine the recovery ratio (RR) of the RO desalination cycle [22]:

$$RR = \frac{M_d}{M_f} \quad (31)$$

In the above equation, M_d is the volumetric flow rate of distilled water and M_f is the volumetric flow rate of feed water.

The volumetric flow rate of brine (M_b) is defined as the following equation [22]:

$$M_b = M_f - M_d \quad (32)$$

To calculate the salt concentration of distilled water (X_d), the following equation is used [22]:

$$X_d = X_f \times (1 - SR) \quad (33)$$

The salt concentration of seawater (X_b) is represented as below [22]:

$$X_b = \frac{M_f \times X_f - M_d \times X_d}{M_b} \quad (34)$$

The average salt concentration is calculated as follows (X_{av}) [22]:

$$X_{av} = \frac{M_f \times X_f - M_b \times X_b}{M_b} \quad (35)$$

The temperature correction factor (TCF) defined in Reverse osmosis desalination is obtained as follows [22]:

$$TCF = \exp\left(2700 \times \left(\frac{1}{T_f} - \frac{1}{298}\right)\right) \quad (36)$$

The average osmosis pressure on the feed (load) side is calculated with the following relation [22]:

$$P_{avg,f} = 37.92 \times (X_f + X_b) \quad (37)$$

The net osmosis pressure across the membrane is defined by [22]:

$$P_{avg,net} = P_{avg,f} - 75.84 \times X_d \quad (38)$$

The net pressure difference across the membrane is defined as [22]:

$$\Delta P_{net} = \left(\frac{M_d}{3600 \times TCF \times FF \times A_e \times n_m \times n_v \times k_w}\right) + P_{avg,net} \quad (39)$$

In the above equation, A_e refers to the area of the element. Also, k_w is the water permeability of the membrane. n_m and n_v are the membrane elements and the number of pressure vessels, respectively.

Also, in order to calculate the pump's electricity consumption, the following relationship is considered [22]:

$$\dot{W}_{RO} = \frac{1000 \times M_f \times \Delta P_{net}}{3600 \times \eta_{is,pump,RO} \times \rho_f} \quad (40)$$

3-4-Analysis of exergy and energy

In this section, regardless of the potential and kinetic energy for each component used in the simulated plant, the energy balance equation is defined as follows [57]:

$$\dot{Q} - \dot{W} = \sum \dot{n}_{out} \bar{h}_{out} - \sum \dot{n}_{in} \bar{h}_{in} \quad (41)$$

Here, $\dot{W}$ is the power and $\dot{Q}$ is the heat transfer rate.

For each component in steady state, the exergy balance is presented as [57]:

$$\dot{E}x_{De} = \sum \left[1 - \frac{T_0}{T_j}\right] \dot{Q}_j - \dot{W}_{cv} + \sum \dot{E}x_{in} - \sum \dot{E}x_{out} \quad (42)$$

Here, T_j represents the temperature of the component boundaries and the destruction exergy is represented by $\dot{E}x_{De}$.

Also, $\dot{E}x_{out}$ represents the exergy of the output streams and $\dot{E}x_{in}$ represents the exergy of the input streams.

The physical and chemical exergy balance and exergy rate are presented as [58, 59]:

$$\dot{E}x = \dot{E}x_{phy} + \dot{E}x_{che} \quad (43)$$

$$\dot{E}x_{phy} = \sum \dot{n}_i[(\bar{h}_i - \bar{h}_o) - T_0(\bar{h}_i - \bar{h}_o)] \quad (44)$$

$$\dot{E}x_{che} = \dot{n}\sum[y_i \times ex_i^{ch,0} + \sum y_i \times \ln y_i] \quad (45)$$

In Equation (45), $ex_i^{ch,0}$ represents the standard chemical exergy of the species. Also, the indices 0 and i represent the reference point and dead point, respectively. The energy and exergy balance of the proposed system components is presented in Table 3.

Table 3: Energy and exergy balance of the multi-generation plant subsystems proposed in the study

	Energy balance	Exergy balance
Brayton		
Gas Turbine 1	$\dot{W}_{GT} + H_6 = H_5$	$\dot{E}_{De,GT} = \dot{E}_5 - \dot{E}_6 - \dot{W}_{GT}$
Compressor 1	$\dot{W}_{com} + H_1 = H_2$	$\dot{E}_{De,com} = \dot{W}_{com} - \dot{E}_2 - \dot{E}_1$
Combustion Chamber	$-0.02\lambda LHV + h_{air} + \lambda h_{fu} - (1+\lambda)h_p = LHV \times \frac{\dot{m}_{fu}}{\dot{M}_{fu}}$	$\dot{E}_{De,CC} = \dot{E}_5 + \dot{E}_{fuel} - \dot{E}_3$
Inverse Brayton		
Gas Turbine 2	$\dot{W}_{GT} + H_8 = H_7$	$\dot{E}_{De,GT} = \dot{E}_7 - \dot{E}_8 - \dot{W}_{GT}$
Compressor 2	$\dot{W}_{com} + H_9 = H_{10}$	$\dot{E}_{De,com} = \dot{W}_{com} - \dot{E}_{10} - \dot{E}_9$
Regenerator	$\dot{Q}_{RG} + H_7 = H_6$	$\dot{E}_{De,RG} = (\dot{E}_7 - \dot{E}_6) - (\dot{E}_3 - \dot{E}_2)$
MED unite		
Heater	$\dot{Q}_{heater} + H_{11} = H_{10}$ $\dot{Q}_{heater} + H_{24} = H_{23}$	$\dot{E}_{De,heater} = (\dot{E}_{10} - \dot{E}_{11}) - (\dot{E}_{23} + \dot{E}_{24})$
Condenser	$\dot{Q}_{cond} + H_{13} = H_{12}$ $\dot{Q}_{cond} + H_{45} = H_{43}$	$\dot{E}_{De,cond} = (\dot{E}_{12} - \dot{E}_{13}) - (\dot{E}_{45} + \dot{E}_{43})$
Effect1	$T_{26} = T_{25} = T_{24} - \Delta T_{effect}$	$\dot{E}_{De,1st} = (\dot{E}_{23} - \dot{E}_{24}) - (\dot{E}_{25} + \dot{E}_{26} - \dot{E}_{22})$
Effect2	$T_{28} = T_{27} = T_{25} - \Delta T_{effect}$	$\dot{E}_{De,2st} = (\dot{E}_{25} - \dot{E}_{27}) - (\dot{E}_{28} + \dot{E}_{29} - \dot{E}_{21} - \dot{E}_{26})$
Effect3	$T_{31} = T_{32} = T_{28} - \Delta T_{effect}$	$\dot{E}_{De,3st} = (\dot{E}_{28} - \dot{E}_{30}) - (\dot{E}_{31} + \dot{E}_{32} - \dot{E}_{29} - \dot{E}_{20})$
Effect4	$T_{34} = T_{35} = T_{31} - \Delta T_{effect}$	$\dot{E}_{De,4st} = (\dot{E}_{31} - \dot{E}_{33}) - (\dot{E}_{34} + \dot{E}_{35} - \dot{E}_{19} - \dot{E}_{32})$
Effect5	$T_{37} = T_{38} = T_{34} - \Delta T_{effect}$	$\dot{E}_{De,5st} = (\dot{E}_{34} - \dot{E}_{36}) - (\dot{E}_{37} + \dot{E}_{38} - \dot{E}_{18} - \dot{E}_{35})$
Effect6	$T_{39} = T_{40} = T_{37} - \Delta T_{effect}$	$\dot{E}_{De,6st} = (\dot{E}_{37} - \dot{E}_{40}) - (\dot{E}_{39} + \dot{E}_{41} - \dot{E}_{17} - \dot{E}_{38})$
Effect7	$T_{43} = T_{44} = T_{39} - \Delta T_{effect}$	$\dot{E}_{De,7st} = (\dot{E}_{39} - \dot{E}_{42}) - (\dot{E}_{43} + \dot{E}_{44} - \dot{E}_{16} - \dot{E}_{41})$

RO unit		
RO	$H_{68} = H_{69} + H_{70}$	$\dot{E}_{De,RO} = \dot{E}_{68} - (\dot{E}_{69} + \dot{E}_{70})$
Refrigeration unit		
Pump	$\dot{W}_{pump} + H_{53} = H_{52}$	$\dot{E}_{De,pump} = \dot{W}_{pump} - (\dot{E}_{53} - \dot{E}_{52})$
Condenser	$\dot{Q}_{cond} + H_{49} = H_{48}$ $\dot{Q}_{cond} + H_{62} = H_{63}$	$\dot{E}_{De,cond} = (\dot{E}_{48} - \dot{E}_{49}) - (\dot{E}_{63} - \dot{E}_{62})$
Generator	$\dot{Q}_{gen} = H_{54} - H_{48} - H_{55}$ $\dot{Q}_{gen} + H_{47} = H_{11}$	$\dot{E}_{De,gen} = (\dot{E}_{11} - \dot{E}_{47}) - (\dot{E}_{48} + \dot{E}_{55} - \dot{E}_{54})$
Absorber	$\dot{Q}_{abs} + H_{66} = H_{67}$ $\dot{Q}_{abs} + H_{52} = H_{51} + H_{57}$	$\dot{E}_{De,abs} = (\dot{E}_{66} - \dot{E}_{65}) - (\dot{E}_{52} + \dot{E}_{58} - \dot{E}_{53})$
Evaporator	$\dot{Q}_{Eva} + H_{60} = H_{59}$ $\dot{Q}_{Eva} + H_{65} = H_{64}$	$\dot{E}_{De,Eva} = (\dot{E}_{59} - \dot{E}_{60}) - (\dot{E}_{64} - \dot{E}_{65})$
Compressor 3	$\dot{W}_{com} + H_{60} = H_{61}$	$\dot{E}_{De,com} = \dot{W}_{com} - (\dot{E}_{61} - \dot{E}_{60})$
E.V1	$H_{50} = H_{49}$	$\dot{E}_{De,E.V1} = \dot{E}_{49} - \dot{E}_{50}$
E.V2	$H_{59} = H_{58}$	$\dot{E}_{De,E.V2} = \dot{E}_{58} - \dot{E}_{59}$
E.V3	$H_{56} = H_{57}$	$\dot{E}_{De,E.V3} = \dot{E}_{56} - \dot{E}_{57}$

3-5-Exergoeconomic analysis

The economic analysis of the proposed system for all components is given in Table 4. The sum of the maintenance cost rate and the investment cost rate equals the total cost rate of each component, which is defined as follows equation [60]:

$$\dot{Z}_k = \dot{Z}_k^{CI} + \dot{Z}_k^{OM} \quad (46)$$

In the above equation, CI refers to investment and OM refers to maintenance. The investment cost rate is obtained by the following equation [60]:

$$\dot{Z}_k^{CI} = \frac{CRF}{\tau} Z_k \quad (47)$$

In this equation, the annual operating hours of the component are denoted by τ. Its unit is hours (h), and its value is taken as 7000 hours per year. The equation related to CRF is defined as the following equation [60]:

$$CRF = \frac{i_r(1+i_r)^n}{(1+i_r)^n - 1} \quad (48)$$

n represents the operating years and i_r represents the interest rate.

The cost rate for maintaining components is calculated using the following equation [60]:

$$\dot{Z}_k^{OM} = \frac{\gamma_k Z_k}{\tau} \quad (49)$$

In the above equation, the system component maintenance factor is represented by γ_k.

Table 4: Investment cost functions of the system's components

Component	Investment cost function
Brayton & inverse Brayton [61]	
Compressor1	$71.1 \times \dot{m}_1 [\frac{1}{0.92 - \eta_{com1}}] R_{com1} \ln(R_{com1})$
Compressor2	$71.1 \times \dot{m}_9 [\frac{1}{0.92 - \eta_{com2}}] R_{com2} \ln(R_{com2})$
Turbine1	$\left(\frac{479.34\dot{m}_4}{0.92 - \eta_{is,GT1}}\right) \ln\left(\frac{P_5}{P_4}\right) [1 + \exp(0.036T_4 - 54.4)]$
Turbine2	$\left(\frac{479.34\dot{m}_7}{0.92 - \eta_{is,GT2}}\right) \ln\left(\frac{P_7}{P_8}\right) [1 + \exp(0.036T_7 - 54.4)]$
CC	$\frac{46.08\dot{m}_{air}}{0.995 - \frac{P_4}{P_6}} [1 + \exp(0.018T_6 - 26.4]$
MED unit [62]	
MED unit	$130 \times (\frac{A}{0.093})^{0.78}$
Refrigeration [52]	
Condenser	$8000 \times (\frac{A_{cond}}{100})^{0.6}$
Generator	$17500 \times (\frac{A_{Gen}}{100})^{0.6}$
Pump	$1120 \times (\dot{W}_{pump})^{0.8}$
Absorber	$16500 \times (\frac{A_{abs}}{100})^{0.6}$
E.V 1	$114.5 \times \dot{m}_{49}$
Evaporator	$16000 \times (\frac{A_{Eva}}{100})^{0.6}$
E.V 2	$114.5 \times \dot{m}_{58}$
E.V 3	$114.5 \times \dot{m}_{56}$
SE [63]	
Stirling engine	$2200 \times P_{SE}$
RO [64]	
RO	$2000 \times (\dot{m}_d)^{0.65}$

3-6-Battery storage

Among the various types of batteries, lithium-ion batteries are widely adopted due to their numerous advantages. Unlike traditional batteries, which use irreversible chemical reactions to generate electricity, lithium batteries are rechargeable because they rely on the movement of lithium ions between two electrodes. This unique feature not only significantly extends the battery's useful life but also helps preserve the environment. Lithium-ion batteries with high energy density can store a significant amount of energy in a compact space. Among the advantages of this battery model are the following [65]:

-Lithium-ion models generally have twice the energy density of nickel-cadmium batteries, and their potential is significantly higher. These batteries have excellent charging characteristics and discharge similarly to nickel-cadmium batteries.

-The high cell voltage (charge difference between the two electrodes) of 3.6 volts allows the use of a single cell in the battery design. A cell is an anode and a cathode separated by an electrolyte. Most mobile phones today use a single-cell battery.

- Lithium-ion batteries require minimal maintenance, making them one of the least maintenance-intensive battery technologies. In addition, lithium-ion batteries exhibit no memory effect and do not require programmed charge–discharge cycles to extend their service life.

- In addition, their self-discharge rate is less than half that of comparable nickel-based batteries, and their environmental impact after disposal is relatively low.

At time t, the battery's state of charge ($SOC^{t}_{battery}$) depends on both the discharged and charged power, as well as its state of charge at time t-1. Additionally, the battery's lower state of charge corresponds to its maximum energy storage capacity. Within the time interval t, the discharged and charged powers are equal to the maximum charged and discharged powers of the battery, respectively. A binary variable representing the on and off states of battery charging and discharging. The on and off states of battery charging and discharging are represented by the binary variables u^{t}_{dis} and u^{t}_{ch}. These variables are defined so that the battery energy storage system cannot operate in both charging and discharging states simultaneously. To charge the battery to less than its maximum power storage capacity ($\overline{E}^{t}_{ch}$), u^{t}_{ch} must equal 1. Otherwise, E^{t}_{ch} becomes zero, resulting in u^{t}_{ch} equal to zero [66].

$$SOC^{t}_{battery} = SOC^{t-1}_{battery} + \eta_{ch} E^{t}_{ch} - \frac{E^{t}_{dis}}{\eta_{dis}} \leq \overline{SOC} \quad (50)$$

$$E^{t}_{ch} \leq u^{t}_{ch} \times \overline{E}_{ch} \quad (51)$$

$$E^{t}_{dis} \leq u^{t}_{dis} \times \overline{E}_{dis} \quad (52)$$

$$u^{t}_{dis} + u^{t}_{ch} \leq 1 \quad (53)$$

3-7-Load management strategy

The amount of electricity purchased from the local distribution grid is influenced by several factors, including electrical loads, demand, battery charging and discharging patterns, and on-site electricity generation. The cost of grid electricity can be reduced when demand response programs (DRPs) are implemented, compared to scenarios without such programs. This reduction, however, is conditional: a portion of the final consumer's electricity demand must be optimally shifted from periods of high tariffs or peak consumption to periods with lower tariffs or off-peak hours. The load management program is modeled using the equations presented in [66].

$$D^{DRP}_{t} = D^{0}_{t} + \Delta d_{t} \quad (54)$$

$$\sum_{t=1}^{T=24} \Delta dt = 0 \quad (55)$$

$$-\overline{DR} \times D^{0}_{t} \leq \Delta d_{t} \leq \overline{DR} \times D^{0}_{t} \quad (56)$$

The demand values before and after applying the load management strategy are represented by D^{0}_{t} and D^{DRP}_{t}, respectively. The maximum potential of the DRP is the limiting factor on the decision

variable for the load change in time interval t. Also, in equation (56), $\overline{DR}$ denotes the maximum percentage change in load per hour relative to the base load. According to relation 55, to ensure partial power outages, the sum of load changes over the study horizon should be zero. This means that the total time period under study is 24 hours, and that, over this period, the sum of load changes must be zero. This means that if the load decreases in one hour, it must have increased in other hours.

3-8-Optimization Problem

Equation (57) is used to minimize the total cost of electricity in an industrial microgrid. The local power distribution grid, denoted by E_{grid}^{t}, has a negative or positive value. The total power generated by the power plant, including the discharged battery power at time t, will be less than the end-user demand when $0 < E_{grid}^{t}$. A negative value indicates that the battery-generated electricity exceeds the load level. Therefore, to make a profit, at a given time yield, the excess electricity generated can be sold to the local power grid.

In the optimization problem, the goal is to minimize the cost of electricity purchased from the local power distribution grid in a day (24-hour period). Therefore, because power prices fluctuate hourly, the amount of power purchased from the grid per hour must be multiplied by its price and included in the objective function with a positive sign (imposing the cost of purchasing power on the microgrid owner). In an hour when the generated power (the amount of power discharged from the battery plus the net amount of power generated by the system) is greater than the consumer's power demand, then the excess power is sold to the local power distribution grid during that hour, and income is earned from the sale of power. As a result, the income earned in that hour will be treated as the objective function, with a negative sign. To calculate the net cost of the microgrid, the total costs are subtracted from the total income from exchanging power with the power distribution grid over a 24-hour period.

$$\text{objective function} = \min \sum_{t=1}^{T} \lambda_{E}^{t} E_{grid}^{t} \quad (57)$$

In equation (57), λ_{E}^{t} refers to the price of buying or selling power to the local power distribution grid, its unit is \$/kWh. Also, E_{grid}^{t} is the power purchased from the local power distribution system at time t. Also, its unit is kW. During each time interval t, the electrical demand should be equal to or less than those generated by this multi-generation unit, as exposed in (58):

$$E_{grid}^{t} + E_{dis}^{t} + \dot{W}_{net} \geq D_{E}^{t} + E_{ch}^{t} \quad (58)$$

3-9-Performance relations

This section presents the parameters describing the proposed system, applying the laws of thermodynamics. The Gain output ratio (GOR) is one of the characteristics of desalination plants, the relationship of which is defined according to the following equation:

$$GOR = \frac{\dot{m}_{fw}}{\dot{m}_{st}} \quad (59)$$

In the above relationship, $\dot{m}_{fw}$ represents the mass flow rate ratio of produced freshwater and $\dot{m}_{st}$ represents the fed steam .

The following performance parameter is the amount of work produced, which is defined according to the proposed system as follows:

$$\dot{W}_{net,total} = \dot{W}_{GT1} + \dot{W}_{GT2} - \dot{W}_{com1} - \dot{W}_{com2} - \dot{W}_{com3} - \dot{W}_{Pump} \quad (60)$$

The first and second law efficiencies for a multiple production system are defined in terms of the following relationships:

$$\eta_{energy} = \frac{\dot{W}_{net,total} + (\dot{m}_{46} \times h_{fg,fw}) + (\dot{m}_{70} \times h_{fg,fw}) + \dot{Q}_{cooling}}{\dot{Q}_{CC}} \times 100 \quad (61)$$

$$\eta_{exergy} = \frac{\dot{E}x_{p,total}}{\dot{E}x_{fu,total}} \times 100 \quad (62)$$

The total investment cost rate for a multi-generation cycle is obtained through the following relationship:

$$\dot{Z}_{total} = \sum_{k-1}^{n} \dot{Z}_{k,PY} \quad (63)$$

3-10-Environmental analysis

The carbon dioxide emission index (kg/MWh) is a measure of the environmental damage caused by the proposed cycle. In order to obtain the carbon dioxide emission index, the following relationship is defined:

$$CDER = \frac{\dot{m}_{CO_2}}{\dot{W}_{net,total} + (\dot{m}_{46} \times h_{fg,fw}) + (\dot{m}_{70} \times h_{fg,fw}) + \dot{Q}_{cooling}} \times 3600 \times 10^3 \quad (64)$$

In equation (64), the unit of carbon dioxide mass flow rate and freshwater mass flow rate is kg/s. Also, the units of net power and $h_{fg,fw}$ are kW and kJ/kg, respectively.

4- Results and discussion

4-1-Validation

Using EES software to simulate the proposed hybrid power plant, the results for Brayton cycle, MED, SE and RO desalination were compared with previous studies in Table 5. It is worth noting that the MED system is compared with the Rostamzadeh et al. [47] Brayton cycle with Ata [67], the Stirling engine with Kaushik and Kumar [63], and RO desalination with Nafey et al. [68]. A statistical comparison of the MED, Brayton, Stirling, and RO subsystems indicates that the RMSE values range from 3.54% to 6.61%, while the MAPE remains below 6.1% in all cases, and the mean percentage deviation is approximately ±6%. All key performance indicators are also confined within a ±10% deviation band. The results of this comparison are illustrated in Figures 3 and 4. Accordingly, the developed model demonstrates adequate performance prediction and evaluation capabilities and can be considered reliable for conducting design-oriented parametric studies.

Table 5: Validation of the proposed cycle units with previous studies

Parameter	Proposed model	Previous model	Unit
Validation of multi-effect distillation desalination cycle [47].			
Distilled water	79.48	81.75	m^3/h
Gained Output Ratio	5.528	5.73	-
performance ratio	8.69	9.64	-
Validation of Brayton cycle [67]			
Exergy efficiency	0.453	0.4798	%
Thermal efficiency	0.371	0.3821	%
Gas turbine power	2688	2972	kW
Validation of Stirling cycle [63].			
maximum power output	34.48	32.10	kW
Energy efficiency	37.58	37.46	%
Exergy efficiency	56.23	56.19	%
Validation of RO cycle [68].			
Specific power consumption	7.5	7.68	(kWh/m^3)
Recovery ratio	28	30	%
HPP consumption power	1128	1131	kW
Rejected salt concentration	64185	64180	ppm

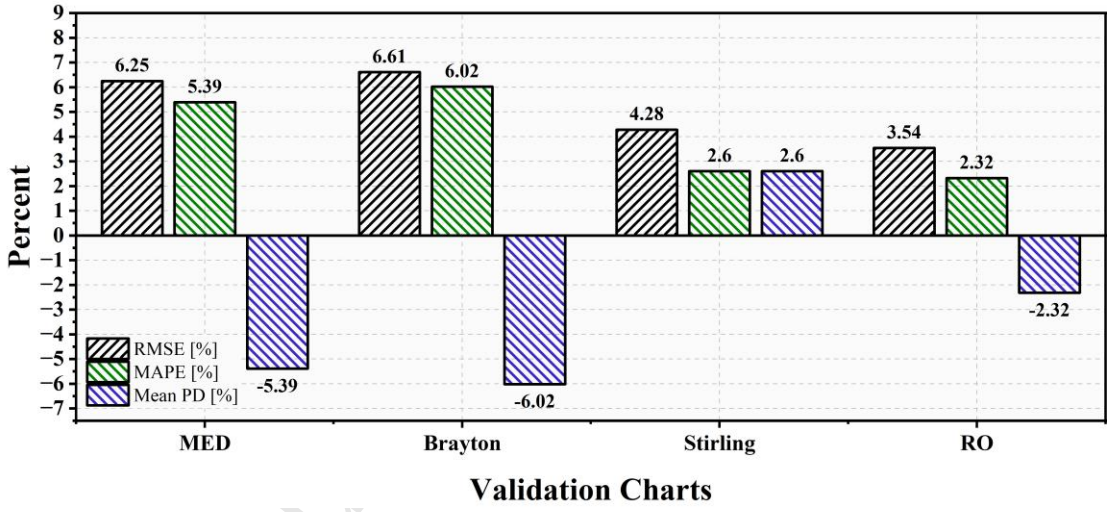

Figure 3: Comparison of model accuracy evaluation indices (RMSE, MAPE, and MPD) for MED, Brayton, Stirling engine, and RO cycles

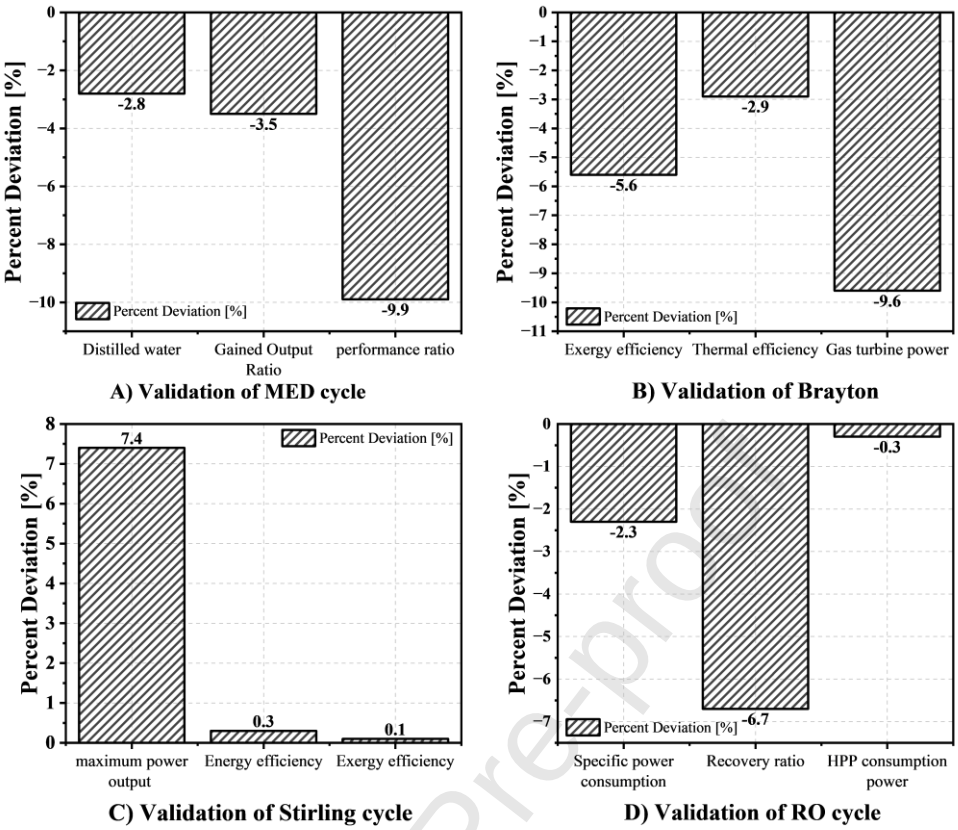

Figure 4: Model validation based on percentage deviation of performance outputs in (A) MED, (B) Brayton cycle, (C) Stirling cycle and (D) RO cycles

4-2- Modeling results

The exergy flow balance for the proposed plant is presented as a Grossman diagram in Figure 5. According to Figure 5, the total exergy of the fuel entering the system equals 3886.56 kW. Among the system components, the combustor in the Brayton cycle unit exhibits the highest exergy destruction rate, at 1055 kW. This significant exergy destruction is primarily attributed to the irreversibility occurring in the combustor. The Stirling engine, with an exergy destruction rate of 257.09 kW, is the second main source of exergy destruction. This is because the heat transfer between the cold and hot cylinder regions in the Stirling engine is high. Also, the temperature difference between the fluid and the source is large, leading to significant exergy destruction. Additionally, 199.1 kW of exergy is ultimately lost through wastewater discharge and heat losses associated with the exhaust gases.

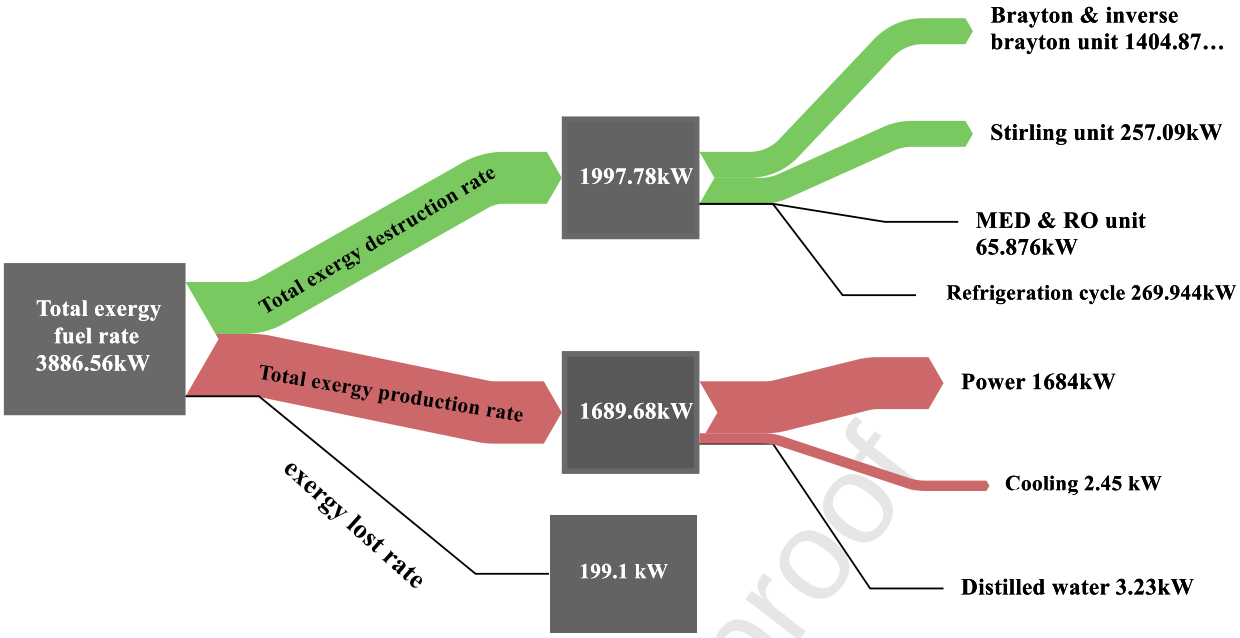

Figure 5: Grossman diagram of exergy for the proposed cycles of the multi-generation system

In Table 6, the fuel exergy, production and destruction of the components used in the proposed cycle are presented. It shows that the Brayton and inverse Brayton cycles achieve high exergy efficiencies, with gas turbines exceeding 94% and compressors mostly above 90%, indicating efficient energy conversion in the power generation components. In contrast, components such as the combustion chamber and certain refrigeration units exhibit lower exergy efficiencies (as low as 40–45%), highlighting significant exergy destruction in these processes. The MED and RO units demonstrate moderate to high exergy efficiencies, with the effects in the MED unit ranging from approximately 72% to 84% and the RO unit achieving over 92%, reflecting effective utilization of thermal and mechanical energy for desalination.

Table 5: Validation of the proposed cycle units with previous

Parameter	Proposed model	Previous model	Unit
Validation of multi-effect distillation desalination cycle [47].			
Distilled water	79.48	81.75	m^3/h
Gained Output Ratio	5.528	5.73	-
performance ratio	8.69	9.64	-
Validation of Brayton cycle [67].			
Exergy efficiency	0.453	0.4798	%
Thermal efficiency	0.371	0.3821	%
Gas turbine power	2688	2972	kW
Validation of Stirling cycle [63].			
maximum power output	34.48	32.10	kW
Energy efficiency	37.58	37.46	%
Exergy efficiency	56.23	56.19	%
Validation of RO cycle [68].			
Specific power consumption	7.5	7.68	kWh/m^3
Recovery ratio	28	30	%
HPP consumption power	1128	1131	kW

Rejected salt concentration	64185	64180	ppm

Table 6: Characteristics of fuel exergy, product exergy, destruction exergy, and exergy efficiency of the components of the proposed multi-generation system

Components	$\dot{E}x_{fu}$(kW)	$\dot{E}x_{p}$(kW)	$\dot{E}x_{De}$(kW)	η_{ex}(%)
Brayton				
Gas Turbine 1	895.1	857	38.1	95.74
Air Compressor 1	1302	1206	96	92.62
Combustion Chamber	4559	3504	1055	76.85
Inverse Brayton				
Gas Turbine 2	1583	1490	93	94.12
Compressor 2	87.42	51.74	35.68	59.18
Regenerator	291.1	236.3	54.8	81.17
Heat exchanger	76.3	44.01	32.29	57.68
MED unite				
Heater	46.85	25.46	21.39	54.34
Condenser	16.28	8.817	7.466	54.15
Effect1	48.61	40.66	7.95	83.64
Effect2	34.92	28.68	6.24	82.13
Effect3	21.74	16.21	5.53	74.56
Effect4	19.03	14.16	4.87	74.40
Effect5	16.74	13.13	3.61	78.43
Effect6	12.82	9.86	2.96	76.91
Effect7	9.2	6.67	2.53	72.5
RO unit				
RO	42.94	39.61	3.33	92.24
Refrigeration unit				
Pump	3.456	2.945	0.511	85.21
Condenser2	28.248	15.26	12.988	54.02
Generator	68.073	32.954	35.119	43.40
Absorber	19.53	8.35	11.18	42.75
Evaporator1	102.27	88.127	14.143	86.17
Compressor	276.12	145.74	130.38	52.78
E. V1	55.58	37.457	18.123	67.39
E. V2	4.57	1.835	2.735	40.153
E. V3	3.86	1.69	2.17	43.78
Evaporator2	73.56	56.24	17.32	76.45
Condenser3	27.25	15.965	11.285	58.58
Heat exchanger	33.35	19.36	13.99	58.05

Table 7: Technical specifications of battery and DSM program

Parameter	Amount	Unit
SOC	1	MW
E_{ch}	1	MW
E_{dis}	1	MW
$\overline{DR}$	0.16	%
η_{ch}	0.95	%
η_{dis}	0.95	%

In the proposed system, a 24-hour case study is conducted to evaluate its performance. In this study, two scenarios are considered: one without DSM and a battery, and the other with DSM and a battery. Also, the consumer is an industrial consumer. The system parameters, which include

several fixed values, are listed in Table 7. In this study, $\overline{DR}$ equals 16%, meaning that hourly demand changes must be less than 16% of the base load in that hour. The global electricity price over a 24-hour summer day is shown in Figure 6.

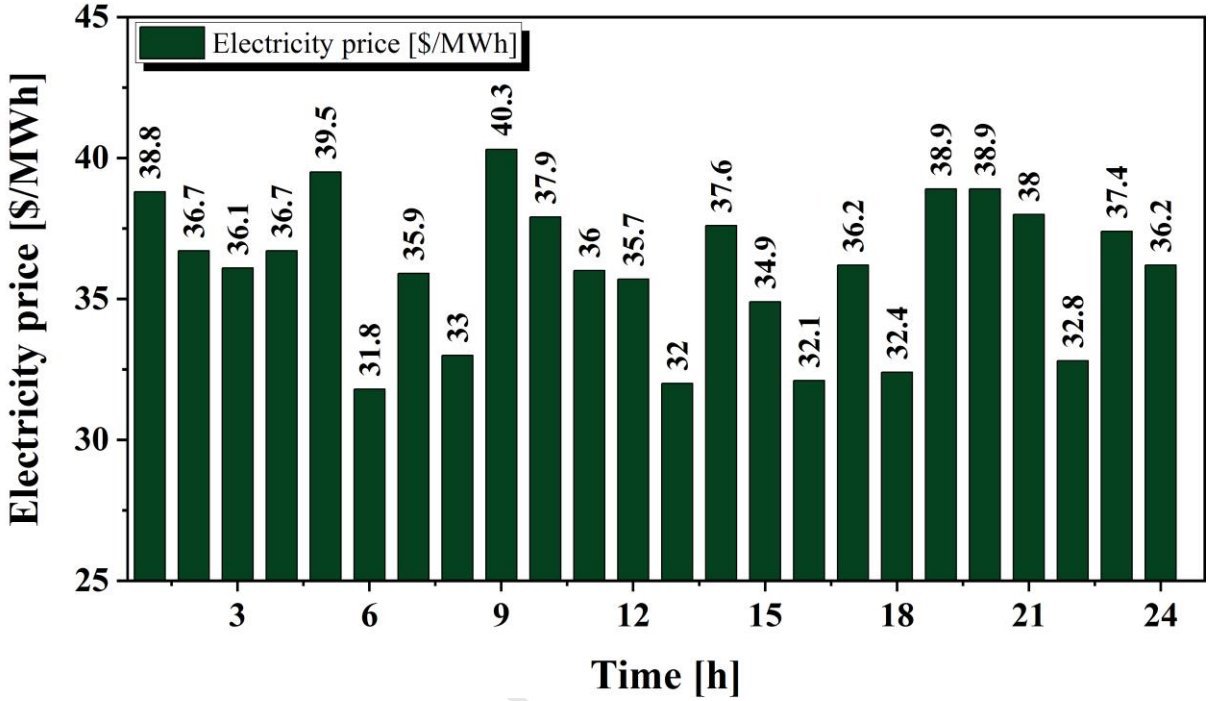

Figure 6: Local electricity prices during a 24-hour sample summer day [65]

Figures 7-10 related to energy consumption management have been analyzed with GAMS optimization software. Two scenarios, one without and one with DSM and battery, are studied to demonstrate the robustness and cost-effectiveness of a storage and demand response scheme in the energy procurement process. The hourly electrical power purchased from the local electricity distribution company is shown in Figure 7. The negative value represents the surplus power, which is sold to the power distribution grid. When this value is positive, it indicates that power is being purchased from the local distribution grid and a power shortage exists.

For two consecutive hours, 13 and 14, the interpretation of Figures 7-10 is as follows. Based on Figure 7, at 13:00, after applying DSM and battery, the load purchased from the grid is 2263.5 kW. At the next hour, i.e., at 14:00, as shown in Figure 7, the electrical power purchased from the local distribution grid is negative and 382.1 kW of power is sold to the grid. According to Figures 9 and 10, at 13:00, the battery is charged, with a charging power of 1000 kW. At this hour, the battery SOC is 950 kW, and the battery is fully charged. At 14:00, the battery is discharged to 902.5 kW, and the battery SOC value reaches 0 kW. According to Figure 8, the electrical demand at 13:00 is 2787.7 kW. Also, the electrical demand at 14:00 is 2049.6 kW.The power generation at 13:00 is calculated to be 1524.2 kW using equation (58). Therefore, at 13:00, the system's electricity demand is at its peak, and both electricity is purchased from the grid, and the battery is charged. At 14:00,

demand decreased, at which time the battery began to discharge, supplying part of the load and selling excess power to the grid.

After adding a battery and DSM, and based on the power balance equation (58) with a one-hour time step, the system performance at hours 6 and 9 in the morning can be analyzed as follows. At 6:00 (see Figure 8), the electrical demand is 1742.80 kW. During this hour, the battery is charging at 1000.00 kW, with no discharging. In comparison, at 9:00, the electrical demand decreases to 1561.10 kW, the battery is discharging at 950.00 kW, and no charging occurs. According to Figure 7, at 6:00, the system buys 1258.00 kW from the grid, with no power sold. At 9 o'clock, the grid power value is 891.60 kW, indicating that 891.60 kW is sold to the grid, with no purchase from it. As a result, the battery SOC increases to 950.00 kW at 6:00 and the net generated power, based on energy balance, is 1484.80 kW. At 9:00, battery discharge reduces the SOC to 0.00 kW, and the net generated power is 1502.70 kW from the balance equation. This sequence can be used for analysis at other hours as well. This behavior well reflects the coordination between the load management strategy and the battery performance in reducing costs and optimizing energy exchange with the grid.

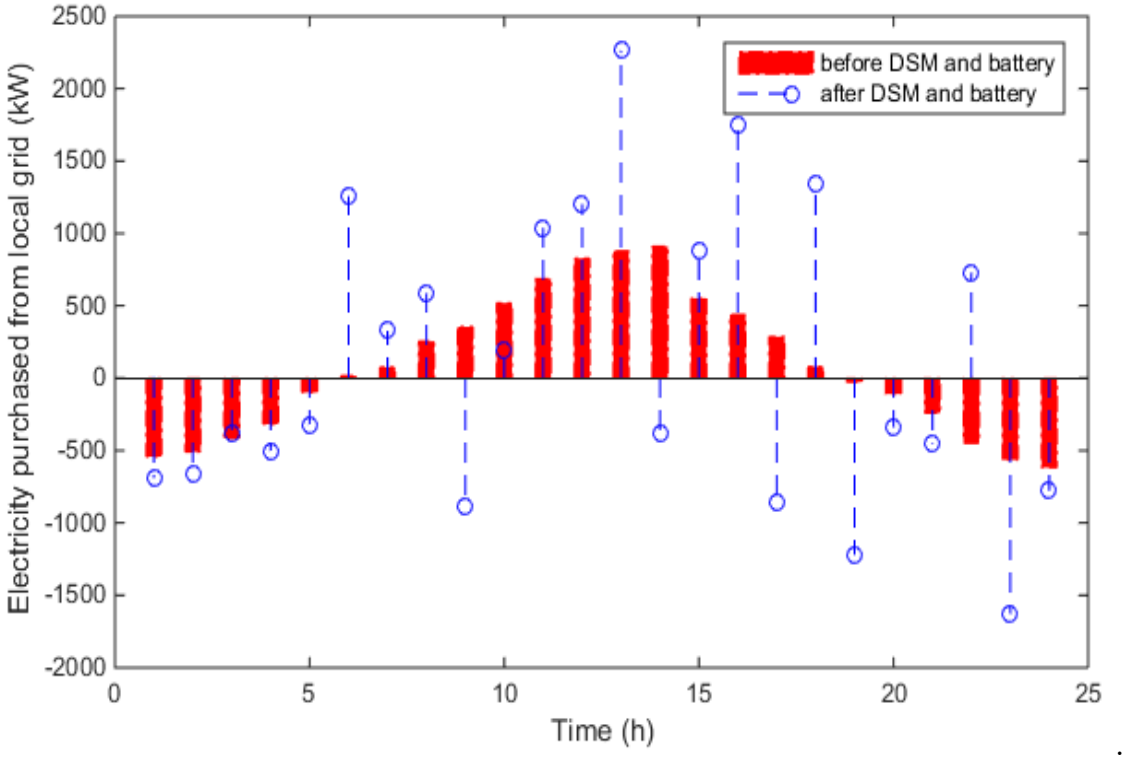

Figure 7: Electrical power purchased from the local grid before and after DSM and battery energy storage application

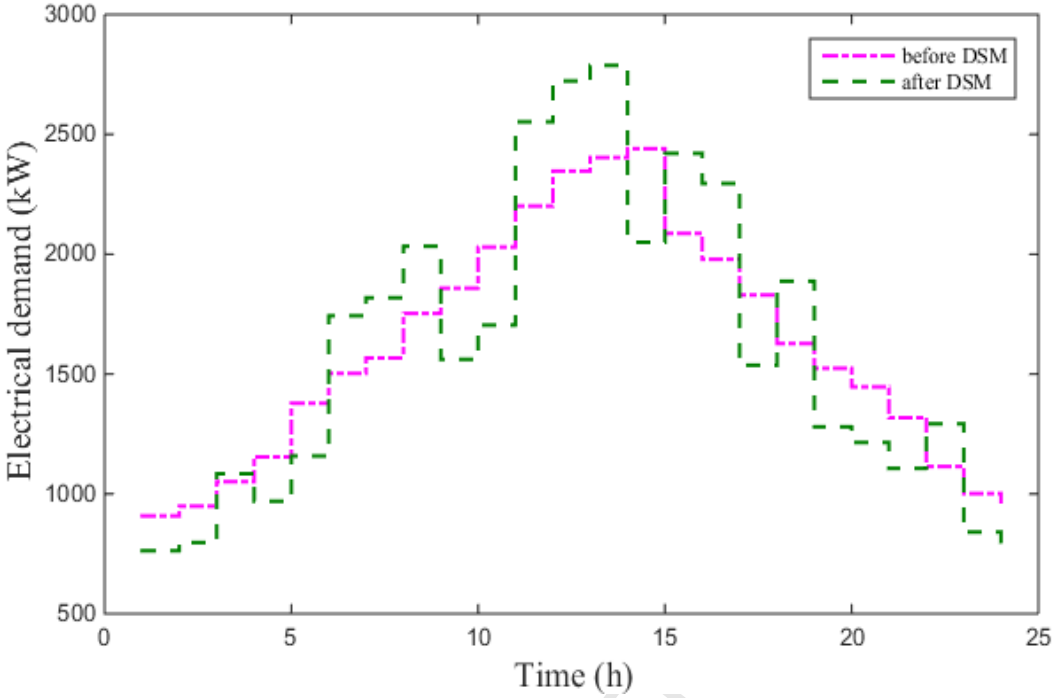

Figure 8: Optimal daily pattern of electricity demand before and after DSM application

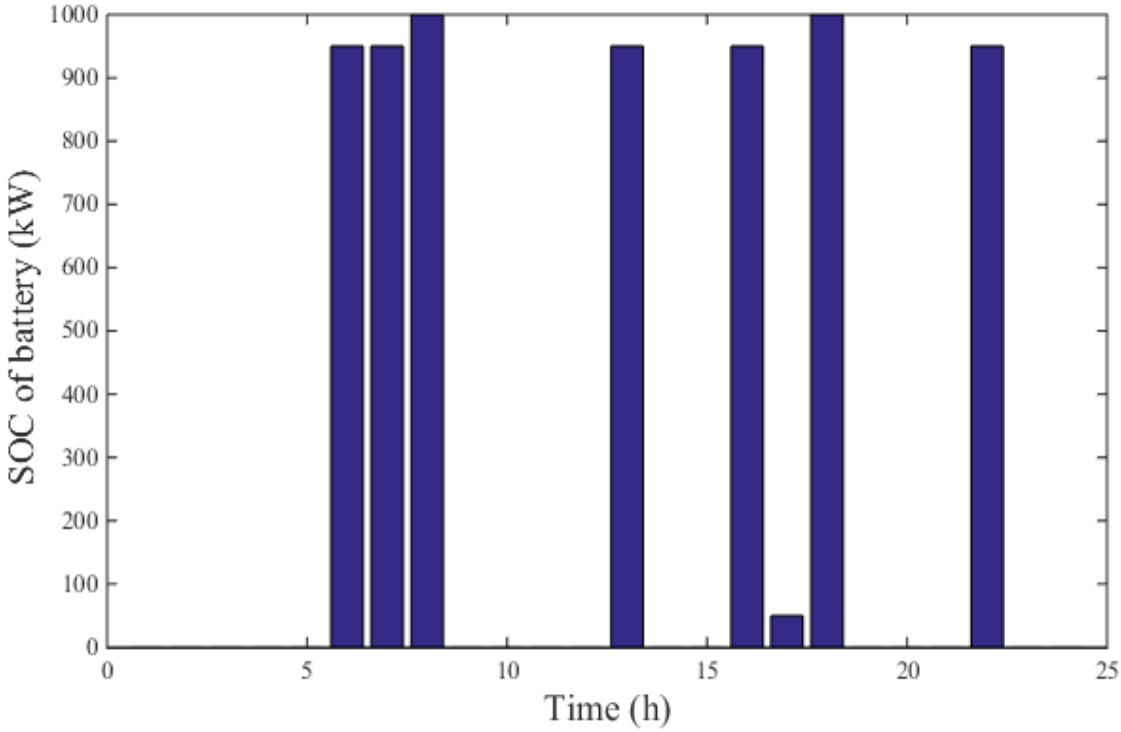

Figure 9: State of charge of battery energy storage during a 24-hour

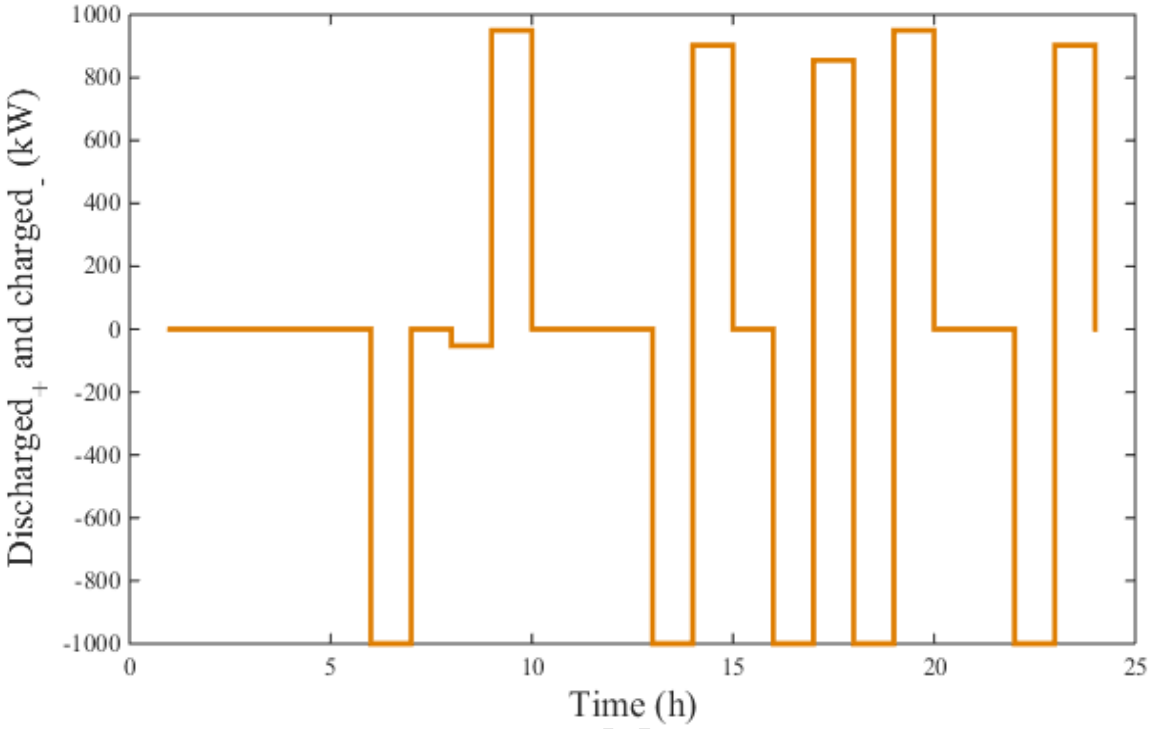

Figure 10: Daily charge- and discharge+ pattern of battery energy storage

4-3-Parametric study

This section presents a detailed analysis of how the main design parameters of the proposed power plant influence its performance, considering aspects such as total cost, power generation, exergy efficiency, and energy efficiency. The design parameters considered in this study are the combustion chamber inlet temperature, the Brayton cycle turbine inlet temperature, the compressor pressure ratio, and the Brayton cycle turbine pressure ratio.

4-3-1- Behavior of combined cycle performance with varying inlet air temperature to the combustion chamber

Figure 11 illustrates the impact of increasing the temperature of point 3 on the power output, energy efficiency, exergy efficiency, and overall cost rate of the studied system. Increasing the temperature upstream of the combustor, while maintaining a constant fuel flow, increases waste heat. This results in the gas turbine producing more power. However, this also increases the power consumption of the compressor. As a result, the net power output is determined by the gas turbine work minus the compressor work. On the other hand, increasing the temperature at point 3 reduces the temperature of the gas cooled by the regenerator. This reduces the temperature of the gases leaving the inverse Brayton cycle. As a result, less heat is supplied to the SE, leading to a reduction in its operating temperature and power output. The net power, defined as the gas turbine power minus the compressor power plus the work produced by the Stirling engine, is reduced. As a result, this effect reduces the net power output of the proposed cycle from 1684 kW to 1638 kW. Additionally, as the temperature at point 3 increases, the heat supplied by the biogas fuel decreases,

resulting in an increase in energy efficiency from 51.57% to 59.13%. Additionally, for the analysis of exergy efficiency, it can be observed that as the temperature at point 3 increases, the exergy of the fuel entering the combustion chamber decreases, while the exergy efficiency increases from 50.84% to 58.4%. As the temperature at point 3 increases, the overall cost rate rises from 24.93 $/GJ to 26.17 $/GJ due to the reduction in the heat transfer cross-sectional area.

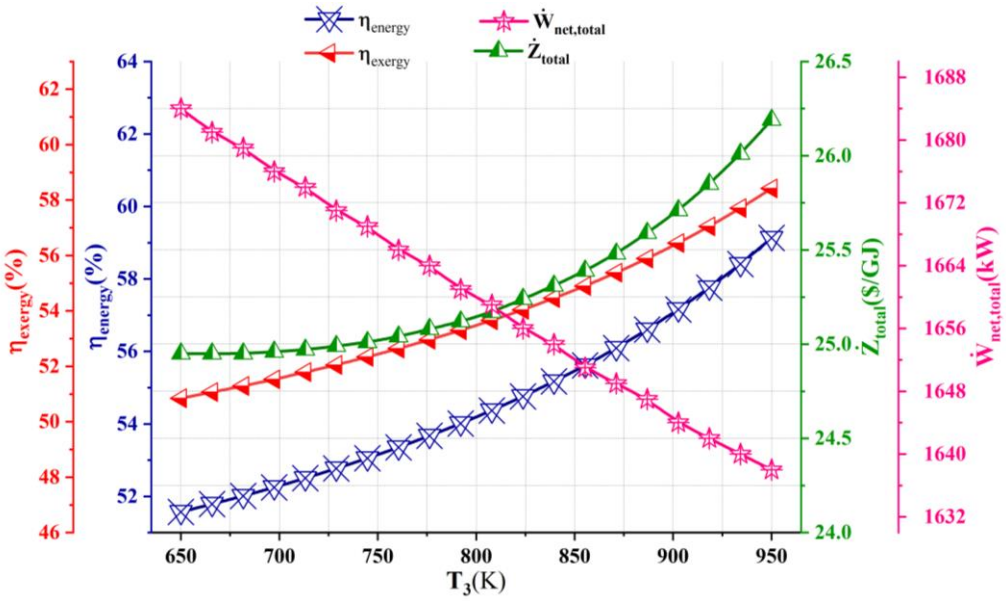

Figure 11: The effect of increasing the Brayton cycle combustion chamber inlet temperature on the net power output, energy efficiency, exergy efficiency and overall cost rate of the proposed system

4-3-2- Behavior of multi-generation performance parameters with varying the Brayton cycle gas turbine inlet temperature

Figure 12 shows the effect of increasing the temperature at point 5 (from 1300 K to 1500 K) on the system performance. Increasing the gas turbine inlet temperature increases the enthalpy difference across the turbine and raises the net power output from 1684 kW to 1723 kW, mainly due to higher turbine work and a larger difference between turbine power output and compressor power consumption. On the other hand, increasing the temperature at point 5 raises the exhaust-gas temperature of the inverse Brayton cycle. For this reason, the SE also recovers more heat, further increasing its output work. The Energy efficiency increases from 51.57% to 53.6%, driven by the reduced heat input to the combustion chamber and higher net power output. The exergy efficiency also increases from 50.84% to 52.78%, since the exergy of the combustion products increases despite the decrease in the fuel exergy. However, the overall cost rate increases from 24.93 $/GJ to 25.22 $/GJ. In the temperature range of 1300 K to 1400 K, the overall cost rate decreases as the compressor investment cost decreases. On the other hand, at temperatures above 1400 K, the system's overall cost rate increases more. This is because the overall cost rate for the generator and heat exchangers increases.

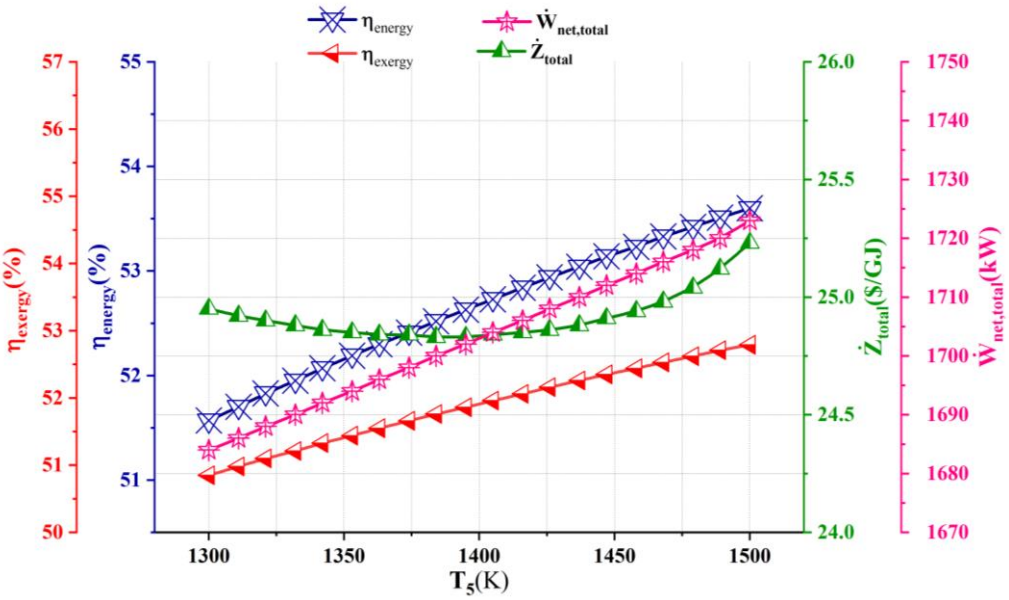

Figure 12: the Effect of increasing the inlet temperature of the Brayton cycle gas turbine on the net power output, energy efficiency, exergy efficiency and overall cost rate of the proposed system

4-3-3- Behavior of multi-generation performance parameters with varying pressure ratio of compressor 1

The effect of changing the pressure ratio of the Brayton cycle compressor (R_{com1}) on the system performance is shown in Figure 13. In the proposed cycle, the GTC's output power remains constant at 1000 kW. Increasing the compressor pressure ratio reduces the exhaust gas temperature. On the one hand, this leads to a decrease in the output power of the inverse Brayton cycle. On the other hand, the Stirling engine's operating temperature has decreased, and it produces less power. As a result, increasing the compressor pressure ratio has reduced the net power of the proposed cycle. Additionally, an increase in exergy efficiency from 50.84% to 64.37% is observed as the fuel flow entering the Brayton cycle combustion chamber is reduced. Additionally, the heat entering the combustion chamber decreases as the compressor pressure ratio in the Brayton cycle increases, thereby improving energy efficiency. The overall cost rate increases with the compressor pressure ratio, reaching 28.9 $/GJ at a pressure ratio of 15. This increase is mainly attributed to the reduced heat recovery in the heat exchangers and the higher cost associated with the first compressor.

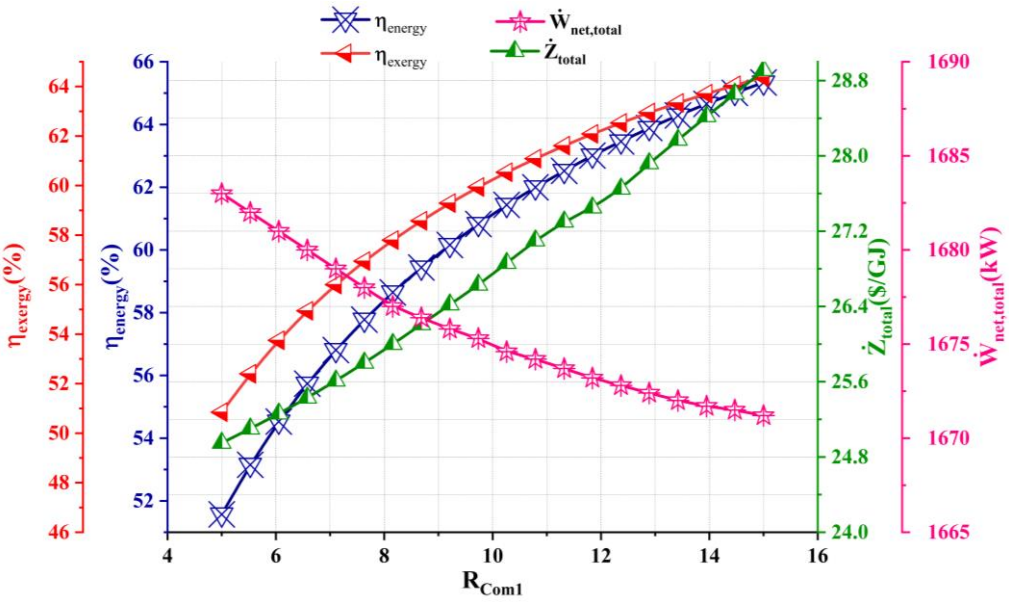

Figure 13: The effect of increasing the pressure ratio of the Brayton cycle compressor on the net power output, energy efficiency, exergy efficiency, and overall cost rate of the proposed system

4-3-4- Behavior of multi-generation performance parameters by varying pressure ratio of compressor 2

According to Figure 14, as the pressure ratio of compressor 2 increases, the work consumed by the compressor surpasses the work produced by the turbines. Additionally, increasing the compressor's pressure ratio reduces the heat recovered by the SE, resulting in lower power output from the SE. Consequently, the overall production capacity of the system decreases. At a pressure ratio of 5, the work output reaches 1643 kW. Additionally, due to the increased heat input to the combustion chamber, the energy efficiency has decreased. The exergy efficiency also decreases due to the lower exergy of the products and the higher exergy of the fuel, reaching 46.68% at a pressure ratio of 5. The overall cost rate has increased to 27.42 $/GJ at a pressure ratio of 5. As the pressure ratio of the second compressor increases, the costs of components such as the second gas turbine and the second compressor also rise. In addition, increasing the heat transfer surface area of the heat exchangers further contributes to the overall cost.

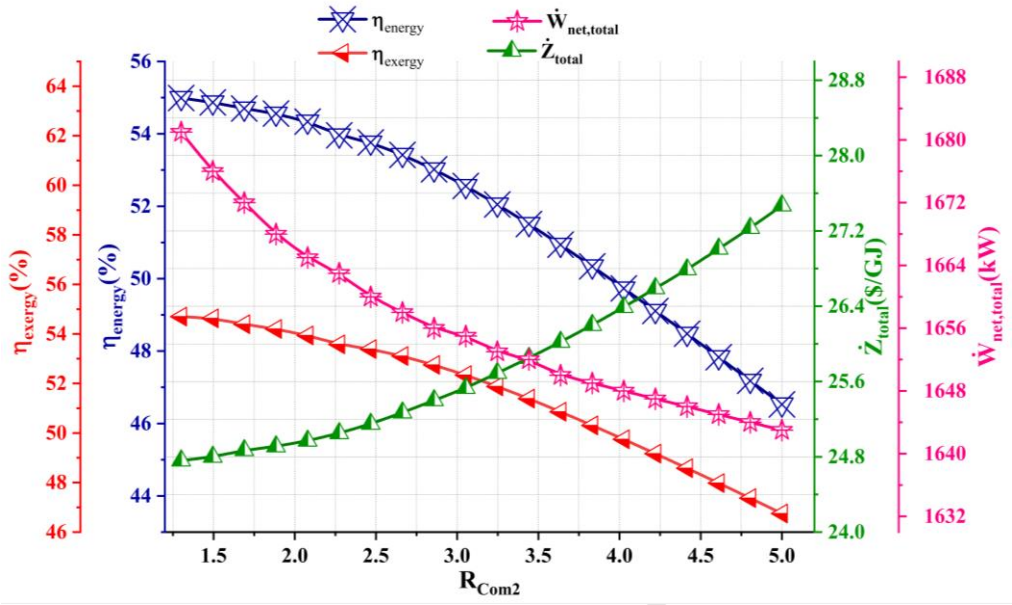

Figure 14: The effect of increasing the pressure ratio of the inverse Brayton cycle compressor on the net power output, energy efficiency, exergy efficiency and overall cost rate of the proposed system

4-3-5- Behavior of multi-generation performance parameters with varying pressure ratio of GT 1

As shown in Figure 15, the work produced by the Brayton cycle turbine increases with the increase in the pressure ratio of the first gas turbine, while the work produced by the inverse Brayton cycle turbine decreases. This further reduces the work input of the Brayton and inverse Brayton cycle compressors. As the gas turbine pressure ratio increases, the exhaust gas temperature decreases. On the other hand, as the exhaust gas temperature decreases, the heat recovery power in the SE decreases. In the end, the net power produced decreases. The heat input to the combustion chamber in the power generation cycle decreases as the gas turbine pressure ratio increases, which explains the increase in energy efficiency. The exergy of the fuel entering the combustion chamber decreases with increasing gas turbine pressure ratio, which increases the exergy efficiency. As the gas turbine pressure ratio increases, the investment cost rate has been declining. Although the overall cost rate shows a downward trend, increasing the gas turbine pressure ratio raises the cost of the first gas turbine, while reducing the costs of other components such as gas turbine 2, compressor 2, and the SE.

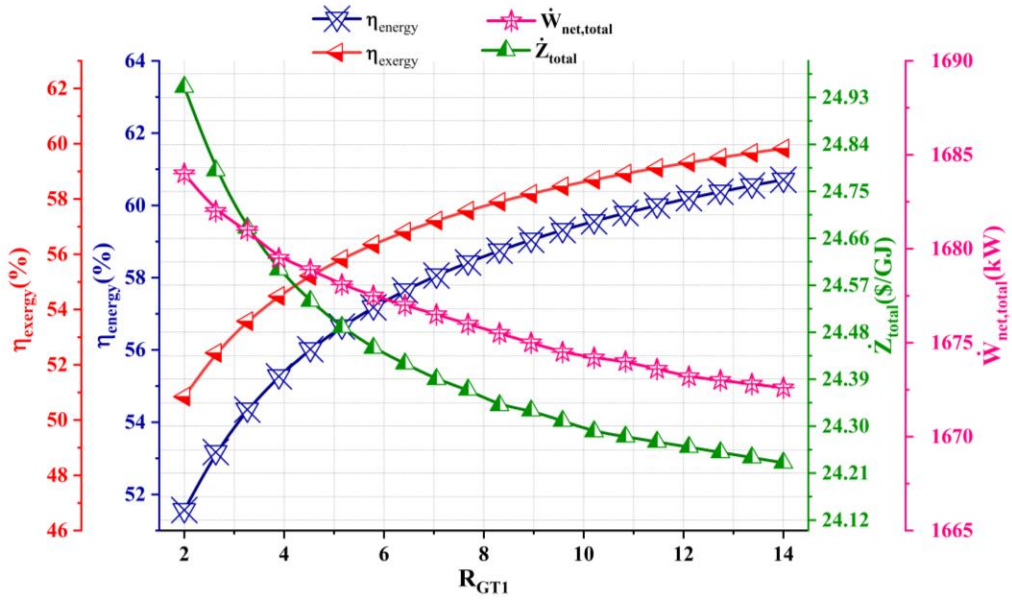

Figure 15: The effect of increasing the GT pressure ratio on the net power output, energy efficiency, exergy efficiency and overall cost rate of the proposed system

The variation of CDER is shown in Figure 16 as a function of design parameters, including R_{GT1}, R_{com1}, R_{com2}, and the inlet and outlet temperatures of the combustion chamber. In the equation defining the carbon dioxide emission rate, the dependent variables are the carbon dioxide production rate and the total product output of the proposed cycle. As shown in Figure 16, the CO_2 emission rate decreases with increasing product output when the temperature at point 5 rises. Furthermore, Figure 16 shows a significant increase in the CO_2 emission rate occurring concurrently with the temperature increase at point 3, which is environmentally detrimental. This increase stems from the corresponding decrease in product output. Increasing the gas turbine pressure ratio reduces the CO_2 emission rate, reaching 282.4 kg/MWh at a pressure ratio of 14. Additionally, the reduction in product output necessitates an increase in the first compressor's pressure ratio within the Brayton cycle, lowering the CO_2 emission rate to 274.5 kg/MWh. However, increasing the inverse Brayton cycle compressor pressure ratio raises the CO_2 emission rate, reaching 309.7 kg/MWh at a pressure ratio of 5.

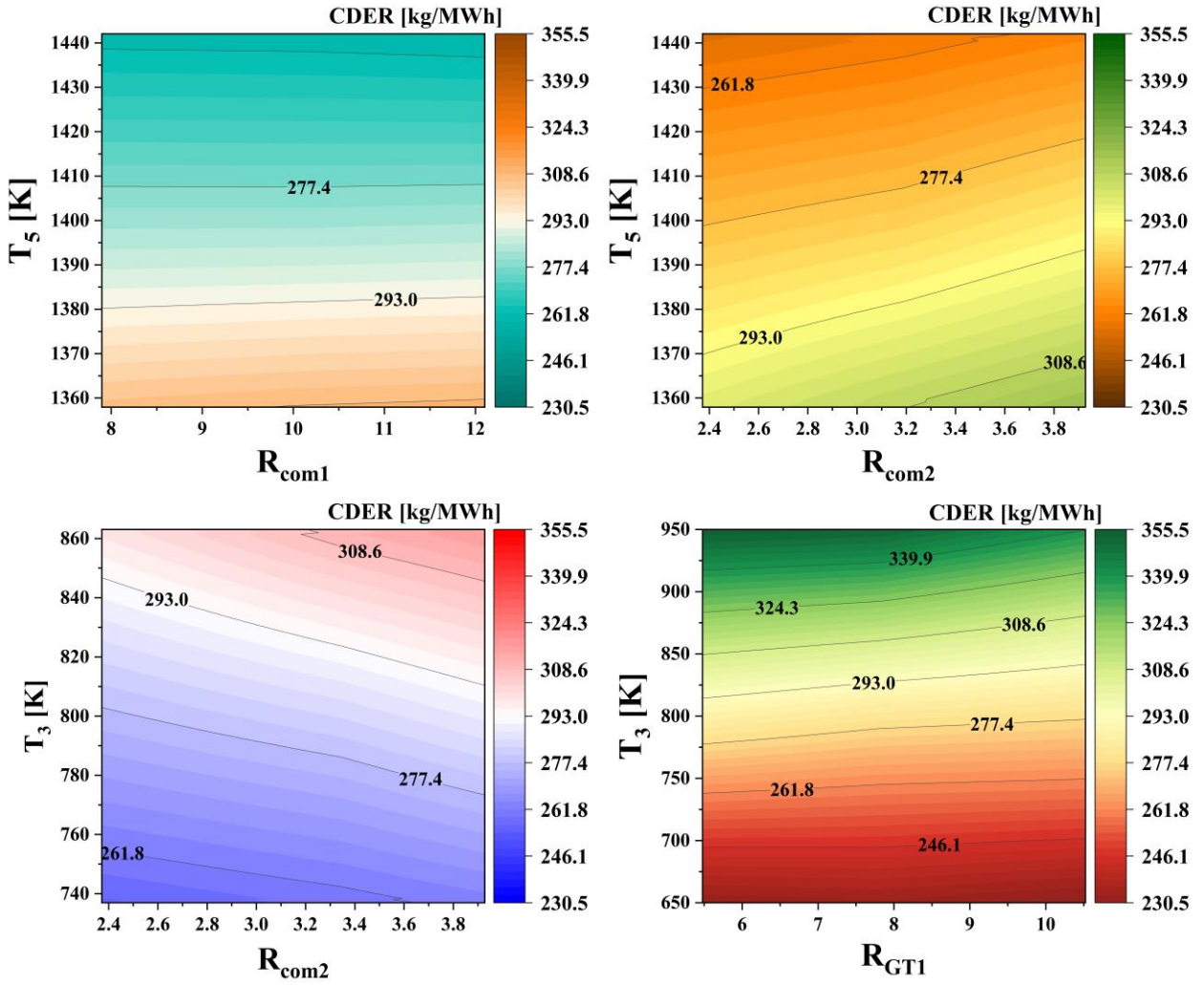

Figure 16: The effect of increasing the design parameters T_5, T_3, R_{com1}, R_{com2}, R_{GT1} on the carbon dioxide emissions of the proposed cycle

5- Conclusion

This study investigated a novel hybrid system for simultaneous power, cooling, and freshwater production. The system integrated a Brayton cycle, an inverse Brayton cycle, a SE, a cascade absorption-condensation refrigeration cycle, RO desalination, and MED. Within this configuration, the inverse Brayton cycle utilizes waste heat from the gas turbine. The SE provided electrical power to the RO unit. Both the MED and RO units produced freshwater. To reduce pollutants and improve efficiency, the Brayton cycle was fueled by biogas. Comprehensive energy, exergy, and economic modeling of the system was conducted using EES software. Optimization of energy consumption management programs was performed using GAMS. Finally, a thermodynamic analysis of the hybrid multi-generation combined-cycle power plant was conducted using fundamental thermodynamic laws. Key simulation results are as follows:

- The energy and exergy efficiencies are calculated to be 51.575% and 50.84%, respectively.

- The net output power, fresh water production rate, and cooling production rate were 1684 kW, 10.404 m^3/h, and 123.56 kW, respectively.
- The highest exergy destruction rate occurred in the Brayton cycle combustion chamber, which was 1055 kW.
- Increasing the temperature of the combustor outlet has a positive effect on the subsystem performance, such that increasing the temperature from 1300 K to 1500 K increases the net power generated from 1684 kW to 1723 kW.
- As the pressure ratio of the air compressor in the Brayton cycle increased, the energy efficiency increased by 13.77%, and the exergy efficiency increased by 13.53%.
- On a very hot summer day, with the battery and DSM strategy in place, the cost of electricity supply was 42 $, compared to 65.80 $ before.

Reference:

[1] M. Ebadollahi, P. Yousefi, and H. Yu, "Inherently safety design of an advanced geothermal-driven triple cooling system: 4E and safety-based optimization framework," *Thermal Science and Engineering Progress,* vol. 67, p. 104117, 2025/11/01/ 2025, doi: https://doi.org/10.1016/j.tsep.2025.104117.

[2] M. Ebadollahi, H. Rostamzadeh, O. Pourali, H. Ghaebi, and M. Amidpour, "Inherently safety design of a dual-loop bi-evaporator combined cooling and power system: 4E and safety based optimization approach," *Process Safety and Environmental Protection,* vol. 154, pp. 393-409, 2021/10/01/ 2021, doi: https://doi.org/10.1016/j.psep.2021.08.036.

[3] M. Abdolalipouradl, F. Mohammadkhani, and M. Yari, "The potential of a novel multigeneration system based on a biogas-fueled gas turbine: Thermodynamic, exergoeconomic, and multi-objective assessments," *Renewable Energy,* p. 123282, 2025.

[4] E. Ersayin and L. Ozgener, "Performance analysis of combined cycle power plants: A case study," *Renewable and Sustainable Energy Reviews,* vol. 43, pp. 832-842, 2015.

[5] Ö. Köse, Y. Koç, and H. Yağlı, "Performance improvement of the bottoming steam Rankine cycle (SRC) and organic Rankine cycle (ORC) systems for a triple combined system using gas turbine (GT) as topping cycle," *Energy Conversion and Management,* vol. 211, p. 112745, 2020.

[6] J. Xie *et al.*, "Analysis of the thermodynamic performance of the SOFC-GT system integrated solar energy based on reverse Brayton cycle," *Energy,* vol. 308, p. 132873, 2024.

[7] M. Zoghi, N. Hosseinzadeh, S. Gharaie, and A. Zare, "Waste heat recovery of a combined Brayton and inverse Brayton cycle for gas turbine based multi-generation hydrogen and freshwater purposes: 4E comparison with a simple coupled Brayton and inverse Brayton cycle," *Thermal Science and Engineering Progress,* vol. 53, p. 102718, 2024.

[8] M. Alabdoadaim, B. Agnew, and I. Potts, "Performance analysis of combined Brayton and inverse Brayton cycles and developed configurations," *Applied thermal engineering,* vol. 26, no. 14-15, pp. 1448-1454, 2006.

[9] L. Chen, D. Ni, Z. Zhang, and F. Sun, "Exergetic performance optimization for new combined intercooled regenerative Brayton and inverse Brayton cycles," *Applied Thermal Engineering,* vol. 102, pp. 447-453, 2016.

[10] D. Di Battista, R. Carapellucci, and R. Cipollone, "Integrated evaluation of Inverted Brayton cycle recovery unit bottomed to a turbocharged diesel engine," *Applied Thermal Engineering,* vol. 175, p. 115353, 2020.

[11] I. Kennedy, Z. Chen, B. Ceen, S. Jones, and C. D. Copeland, "Experimental investigation of an inverted Brayton cycle for exhaust gas energy recovery," *Journal of engineering for gas turbines and power,* vol. 141, no. 3, p. 032301, 2019.
[12] L. Chen, H. Feng, and Y. Ge, "Power and efficiency optimization for open combined regenerative Brayton and inverse Brayton cycles with regeneration before the inverse cycle," *Entropy,* vol. 22, no. 6, p. 677, 2020.
[13] Y. Li *et al.*, "Performance analysis of the Inverted Brayton Cycle in the atmospheric solid oxide fuel cell hybrid power system," *Energy Conversion and Management,* vol. 316, p. 118828, 2024.
[14] M. Ebadollahi, M. Amidpour, O. Pourali, and H. Ghaebi, "Flexibility concept in design of advanced multi-energy carrier systems driven by biogas fuel for sustainable development," *Sustainable Cities and Society,* vol. 86, p. 104121, 2022.
[15] I. Szczygieł, W. Stanek, and J. Szargut, "Application of the Stirling engine driven with cryogenic exergy of LNG (liquefied natural gas) for the production of electricity," *Energy,* vol. 105, pp. 25-31, 2016.
[16] A. Entezari, A. Manizadeh, and R. Ahmadi, "Energetical, exergetical and economical optimization analysis of combined power generation system of gas turbine and Stirling engine," *Energy Conversion and Management,* vol. 159, pp. 189-203, 2018.
[17] A. E. Alali and K. Al Khasawneh, "Performance analysis of stirling engine double-effect absorption chiller hybrid system for waste heat utilization from gas turbine modular helium reactor," *Energy Conversion and Management,* vol. 251, p. 114976, 2022.
[18] D. Ipci and H. Karabulut, "Thermodynamic and dynamic analysis of an alpha type Stirling engine and numerical treatment," *Energy Conversion and Management,* vol. 169, pp. 34-44, 2018.
[19] M. A. Khan, S. Rehman, and F. A. Al-Sulaiman, "A hybrid renewable energy system as a potential energy source for water desalination using reverse osmosis: A review," *Renewable and Sustainable Energy Reviews,* vol. 97, pp. 456-477, 2018.
[20] C. Wang, L. Wang, L. Dong, H. K. Shon, and J. Kim, "Specific energy consumption of seawater reverse osmosis desalination plants using machine learning," *Desalination,* p. 118654, 2025.
[21] Y. Kim, J. Byun, K. Park, and Y.-G. Park, "Comprehensive analysis of energy saving and high-quality permeate production strategies for a large-scale seawater reverse osmosis desalination plant with diverse process configurations and external resource utilization," *Desalination,* vol. 596, p. 118292, 2025.
[22] M. W. Chandio, L. Kumar, A. G. Memon, and M. M. Awad, "Thermodynamic, economic, and environmental evaluation of internal combustion engine exhaust gas-driven Organic Rankine cycles for power generation and desalination," *International Journal of Thermofluids,* vol. 25, p. 101046, 2025.
[23] X. Li *et al.*, "Thermodynamic analysis and optimization of an optimized geothermal-driven quadruple-production system for sustainable power, heat, freshwater, and hydrogen production," *Renewable Energy,* vol. 245, p. 122847, 2025.
[24] W. M. El-Ashmawy, W. M. El-Maghlany, and M. Elhelw, "Thermo-economic analysis of potential desalination processes utilized by no greenhouse gas emissions power plant," *Alexandria Engineering Journal,* vol. 109, pp. 191-200, 2024.
[25] M. W. Shahzad, K. C. Ng, K. Thu, B. B. Saha, and W. G. Chun, "Multi effect desalination and adsorption desalination (MEDAD): A hybrid desalination method," *Applied Thermal Engineering,* vol. 72, no. 2, pp. 289-297, 2014.
[26] N. Chitgar and M. Sadrzadeh, "Optimizing sustainable energy systems: A comparative study of geothermal-powered desalination for green hydrogen production," *Desalination,* vol. 593, p. 118219, 2025.
[27] F. Musharavati, A. Khoshnevisan, S. M. Alirahmi, P. Ahmadi, and S. Khanmohammadi, "Multi-objective optimization of a biomass gasification to generate electricity and desalinated water using Grey Wolf Optimizer and artificial neural network," *Chemosphere,* vol. 287, p. 131980, 2022.

[28] Z. Xu *et al.*, "Design and comprehensive thermo-enviro-economic assessment of an innovative polygeneration system using biomass fuel and LNG regasification: A CCHP-thermally desalination application," *Process Safety and Environmental Protection,* vol. 183, pp. 925-944, 2024.
[29] C. Liu, R. Li, L. Xu, and W. Liu, "A novel mathematical model for mixed-feed multi-effect distillation system optimization design," *Desalination and Water Treatment,* vol. 321, p. 100967, 2025.
[30] H. Jabari, A. S. Ghazani, and F. Jabari, "Techno-economic optimization of a trigeneration system attaining water-heat-energy nexus considering an underground gravity energy storage," *Desalination,* vol. 596, p. 118349, 2025.
[31] Y. Zhang *et al.*, "Real-time global optimal energy management strategy for connected PHEVs based on traffic flow information," *IEEE Transactions on Intelligent Transportation Systems,* 2024.
[32] W. Qi, J. Yang, Z. Zhang, J. Wu, P. Lan, and S. Xiang, "Investigation on thermal management of cylindrical lithium-ion batteries based on interwound cooling belt structure," *Energy Conversion and Management,* vol. 340, p. 119962, 2025.
[33] W. Qi *et al.*, "Multi-U-Style micro-channel in liquid cooling plate for thermal management of power batteries," *Applied Thermal Engineering,* vol. 256, p. 123984, 2024.
[34] M. Goodarzi, "Energy and exergy analyses of a new atmospheric regenerative Brayton and Inverse Brayton cycle," *Energy Reports,* vol. 7, pp. 4530-4539, 2021.
[35] P. Prajapati, V. Patel, B. D. Raja, and H. Jouhara, "Thermal efficiency and specific work optimization of combined Brayton and inverse Brayton cycle: A multi-objective approach," *Thermal Science and Engineering Progress,* vol. 37, p. 101624, 2023.
[36] K. A. Abrosimov, A. Baccioli, and A. Bischi, "Techno-economic analysis of combined inverted Brayton–Organic Rankine cycle for high-temperature waste heat recovery," *Energy Conversion and Management,* vol. 207, p. 112336, 2020.
[37] S. Hou, F. Zhang, and Q. Yang, "Comparative analysis of supercritical CO2–ORC combined cycle for gas turbine waste heat recovery based on multi-objective optimization," *Applied Thermal Engineering,* vol. 236, p. 121776, 2024.
[38] J. Zhou, M. A. Ali, F. M. Zeki, and H. A. Dhahad, "Thermoeconomic investigation and multi-objective optimization of a novel efficient solar tower power plant based on supercritical Brayton cycle with inlet cooling," *Thermal Science and Engineering Progress,* vol. 39, p. 101679, 2023.
[39] Y. Li, L. Wang, S. Sharma, G. Zhang, L. Zhang, and F. Maréchal, "Design and optimization of a solid oxide fuel cell-inverted gas turbine integrated system with zero carbon emission for distributed cogeneration," *Energy Conversion and Management,* vol. 268, p. 116036, 2022.
[40] Y. Yang, Y. Huang, P. Jiang, and Y. Zhu, "Multi-objective optimization of combined cooling, heating, and power systems with supercritical CO2 recompression Brayton cycle," *Applied Energy,* vol. 271, p. 115189, 2020.
[41] J. Nondy and T. Gogoi, "Exergoeconomic and environmental optimization of gas turbine-based CCHP systems: A comprehensive study with multi-objective optimization and decision making," *International Journal of Thermofluids,* vol. 23, p. 100821, 2024.
[42] N. Mahdavi, P. Mojaver, and S. Khalilarya, "Multi-objective optimization of power, CO2 emission and exergy efficiency of a novel solar-assisted CCHP system using RSM and TOPSIS coupled method," *Renewable Energy,* vol. 185, pp. 506-524, 2022.
[43] M. Colakoglu and A. Durmayaz, "Energy, exergy and environmental-based design and multiobjective optimization of a novel solar-driven multi-generation system," *Energy Conversion and Management,* vol. 227, p. 113603, 2021.
[44] I. O. de Paula and L. O. Salviano, "Integration of a power thermal plant under operation to a biomass gasification system: An approach through sensitivity analysis and optimization procedure," *Energy Conversion and Management,* vol. 325, p. 119446, 2025.

[45] J. Liu, C.-Y. Hsu, S. F. Ahmad, M. A. Alotaibi, M. I. Allahham, and M. Qin, "Design and energy, exergy, thermoeconomic, and exergo-environmental (4E) analyses of a novel hybrid geothermal/biogas-powered green multi-generation system using a post-combustion CO2 capture unit," *Applied Energy*, vol. 377, p. 124662, 2025.

[46] F. Yilmaz, M. Ozturk, and R. Selbas, "A parametric examination of the energetic, exergetic, and environmental performances of the geothermal energy-based multigeneration plant for sustainable products," *International Journal of Hydrogen Energy*, vol. 143, pp. 947-957, 2025.

[47] H. Rostamzadeh, H. Ghiasirad, M. Amidpour, and Y. Amidpour, "Performance enhancement of a conventional multi-effect desalination (MED) system by heat pump cycles," *Desalination*, vol. 477, p. 114261, 2020.

[48] T. Gholizadeh, M. Vajdi, and F. Mohammadkhani, "Thermodynamic and thermoeconomic analysis of basic and modified power generation systems fueled by biogas," *Energy conversion and management*, vol. 181, pp. 463-475, 2019.

[49] V. Bakırcıoğlu, H. B. Jond, and F. Yilmaz, "Multi-Objective optimization and thermodynamic analysis of a supercritical CO2 Brayton cycle in a solar-powered multigeneration plant for net-zero emission goals," *Energy Conversion and Management*, vol. 328, p. 119628, 2025.

[50] L. Liu *et al.*, "A novel hybrid biogas–solar-driven energy system integrated with carbon capture for multi-generation: Machine learning-based technical, economic, and environmental optimization," *Applied Thermal Engineering*, p. 128232, 2025.

[51] M. A. Haghghi, S. G. Holagh, A. Chitsaz, and K. Parham, "Thermodynamic assessment of a novel multi-generation solid oxide fuel cell-based system for production of electrical power, cooling, fresh water, and hydrogen," *Energy conversion and management*, vol. 197, p. 111895, 2019.

[52] S. Jafary, S. Khalilarya, A. Shawabkeh, M. Wae-hayee, and M. Hashemian, "A complete energetic and exergetic analysis of a solar powered trigeneration system with two novel organic Rankine cycle (ORC) configurations," *Journal of Cleaner Production*, vol. 281, p. 124552, 2021.

[53] M. Goodarzi, "Comparative energy analysis on a new regenerative Brayton cycle," *Energy Conversion and Management*, vol. 120, pp. 25-31, 2016.

[54] E. Bani-Hani *et al.*, "Energy and exergy analyses of a regenerative Brayton cycle utilizing monochlorobiphenyl wastes as an alternative fuel," *Energy*, vol. 278, p. 127861, 2023.

[55] H. Sayyaadi and A. Saffari, "Thermoeconomic optimization of multi effect distillation desalination systems," *Applied Energy*, vol. 87, no. 4, pp. 1122-1133, 2010.

[56] E. Assareh, M. Jafari, S. Keykhah, and M. Lee, "Transient thermodynamic modeling and economic assessment of cogeneration system based on compressed air energy storage and multi-effect desalination," *Journal of Energy Storage*, vol. 55, p. 105683, 2022.

[57] M. Ebadollahi, B. Shahbazi, and H. Ghaebi, "Efficiency and flexibility enhancement of nanofluid-based hybrid solar desalination system equipped with thermoelectric generator for eco-friendly freshwater and power cogeneration," *Process Safety and Environmental Protection*, vol. 190, pp. 108-122, 2024.

[58] M.-M. Pazuki, M.-R. Kolahi, M. Ebadollahi, and M. Amidpour, "Enhancing efficiency in an innovative geothermal poly-generation system for electricity, cooling, and freshwater production through integrated multi-objective optimization: A holistic approach to energy, exergy, and enviroeconomic effects," *Energy*, vol. 313, p. 133862, 2024.

[59] Y. Cao, S. Hamidvand, M. Bezaatpour, M. Ebadollahi, and H. Ghaebi, "Microporous foam, magnetic nanoparticles, and revolutionary tubes: Sophisticated combination of three solar energy materials in flat plate solar collectors," *Solar Energy Materials and Solar Cells*, vol. 235, p. 111464, 2022/01/01/ 2022, doi: https://doi.org/10.1016/j.solmat.2021.111464.

[60] H. Rostamzadeh, M. Ebadollahi, H. Ghaebi, and A. Shokri, "Comparative study of two novel micro-CCHP systems based on organic Rankine cycle and Kalina cycle," *Energy conversion and management*, vol. 183, pp. 210-229, 2019.

[61] Z. Liu, Z. Liu, X. Yang, H. Zhai, and X. Yang, "Advanced exergy and exergoeconomic analysis of a novel liquid carbon dioxide energy storage system," *Energy Conversion and Management,* vol. 205, p. 112391, 2020.
[62] A. Razmi, M. Soltani, M. Tayefeh, M. Torabi, and M. Dusseault, "Thermodynamic analysis of compressed air energy storage (CAES) hybridized with a multi-effect desalination (MED) system," *Energy Conversion and Management,* vol. 199, p. 112047, 2019.
[63] S. Kaushik and S. Kumar, "Finite time thermodynamic evaluation of irreversible Ericsson and Stirling heat engines," *Energy Conversion and Management,* vol. 42, no. 3, pp. 295-312, 2001.
[64] M. Abdelgaied *et al.*, "Performance assessment of solar PV-driven hybrid HDH-RO desalination system integrated with energy recovery units and solar collectors: Theoretical approach," *Energy Conversion and Management,* vol. 239, p. 114215, 2021.
[65] H. Jabari, A. S. Ghazani, and F. Jabari, "Thermodynamic modeling and optimal short-term scheduling of a green H2-fueled combined heat and power generation system for industrial zones," *International Journal of Hydrogen Energy,* vol. 84, pp. 235-245, 2024.
[66] H. Jabari, A. S. Ghazani, and F. Jabari, "Techno-economic optimization of a trigeneration system attaining water-heat-energy nexus considering an underground gravity energy storage," *Desalination,* vol. 596, p. 118349, 2024.
[67] S. Ata, "Comprehensive evaluation of a gas turbine-based multi-generation system for power, heating, cooling, freshwater, hydrogen and ammonia: 4E assessment and multi-objective optimization with RSM desirability approach," *Renewable Energy,* vol. 246, p. 122900, 2025.
[68] A. Nafey and M. Sharaf, "Combined solar organic Rankine cycle with reverse osmosis desalination process: energy, exergy, and cost evaluations," *Renewable Energy,* vol. 35, no. 11, pp. 2571-2580, 2010.

Declaration of interests

☒ The authors declare that they have no known competing financial interests or personal relationships that could have appeared to influence the work reported in this paper.

☐The authors declare the following financial interests/personal relationships which may be considered as potential competing interests:

Highlights:

- Brayton and inverse Brayton cycles integrated in a novel multigeneration system
- Waste heat drives Stirling and RO–MED units to raise freshwater and power output
- System produces 1684 kW power, 123.6 kW cooling, and 10.4 m^3/h freshwater
- Energy–exergy efficiencies reach ~51% with a cost rate of 24.93 $/GJ
- DSM and battery use cut peak electricity generation cost from 65.8 to 42 $